J. Fluid Mech. (1996), vol. 326, pp. 57–90

Miscible displacements in capillary tubes. Part 2. Numerical simulations

By CHING-YAO CHEN AND ECKART MEIBURG

Department of Aerospace Engineering, University of Southern California, Los Angeles, CA 90089-1191, USA

(Received 11 January 1996 and in revised form 6 May 1996)

Numerical simulations are presented which, in conjunction with the accompanying experimental investigation by Petitjeans & Maxworthy (1996), are intended to elucidate the miscible flow that is generated if a fluid of given viscosity and density displaces a second fluid of different such properties in a capillary tube or plane channel. The global features of the flow, such as the fraction of the displaced fluid left behind on the tube walls, are largely controlled by dimensionless quantities in the form of a Péclet number Pe, an Atwood number At, and a gravity parameter. However, further dimensionless parameters that arise from the dependence on the concentration of various physical properties, such as viscosity and the diffusion coefficient, result in significant effects as well.

The simulations identify two distinct Pe regimes, separated by a transitional region. For large values of Pe, typically above $O(10^3)$, a quasi-steady finger forms, which persists for a time of $O(Pe)$ before it starts to decay, and Poiseuille flow and Taylor dispersion are approached asymptotically. Depending on the strength of the gravitational forces, we observe a variety of topologically different streamline patterns, among them some that leak fluid from the finger tip and others with toroidal recirculation regions inside the finger. Simulations that account for the experimentally observed dependence of the diffusion coefficient on the concentration show the evolution of fingers that combine steep external concentration layers with smooth concentration fields on the inside. In the small-Pe regime, the flow decays from the start and asymptotically reaches Taylor dispersion after a time of $O(Pe)$.

An attempt was made to evaluate the importance of the Korteweg stresses and the consequences of assuming a divergence-free velocity field. Scaling arguments indicate that these effects should be strongest when steep concentration fronts exist, i.e. at large values of Pe and At. However, when compared to the viscous stresses, Korteweg stresses may be relatively more important at lower values of these parameters, and we cannot exclude the possibility that minor discrepancies observed between simulations and experiments in these parameter regimes are partially due to these extra stresses.

1. Introduction

The present computational investigation intends to shed further light on the experiments reported in the companion paper by Petitjeans & Maxworthy (1996), hereafter referred to as Part 1. Those authors investigate the displacement of a viscous fluid in a capillary tube by another one of different viscosity and density. Various flow regimes are observed as a function of the governing parameters, which consist of the dimensionless velocity in the form of a Péclet number Pe, the viscosity ratio

denoted by an Atwood number At, and a parameter F that represents the ratio of gravitational and viscous forces. The experiments serve to determine the dependence of such global quantities as the fraction of displaced fluid left behind on the tube walls on these parameters. In Part 1 it is demonstrated that the finger tip can display fundamentally different dynamics in the various parameter regimes, in analogy to earlier suggestions by Taylor (1961) for the case of immiscible fluids. For example, the experiments show the formation of a 'needle' protruding from the finger tip if less than half of the displaced fluid stays behind on the tube walls.

The numerical simulations to be reported below are intended to provide us with detailed information on the spatio-temporal development of the velocity and concentration fields, and thereby to supplement the experimentally obtained data, and to aid in their understanding and interpretation. The combined information extracted from experiments and simulations, in turn, can serve as a basis for the derivation and validation of a number of scaling laws. These scaling laws will be applicable in various limits of the governing parameters, which leads to a description of disctinctly different flow regimes, particularly in terms of the Péclet number. Eventually, the scaling arguments derived here are expected to bring us closer to the development of the kind of simplified models needed for large-scale miscible two-phase porous-media flow simulations.

Numerical simulations can furthermore be helpful in the evaluation of the importance of those physical effects that are not included in the computational model, but that may be present in the real flow. For the present situation of incompressible, miscible two-phase flows, Joseph (1990) and coworkers (Joseph & Renardy 1993, and references therein) have pointed out the potential significance of additional stresses due to concentration gradients, as first discussed by Korteweg (1901). They furthermore emphasize that the assumption of vanishing divergence of the velocity field holds only approximately, even if the diffusion of the fluids into each other does not result in a volume change. Neither of these effects is included in our numerical simulations, so that the level of agreement with the experimental observations can provide an indication of their importance for the particular flow under consideration.

The outine of the paper is as follows. In §2, we formulate the governing equations in non-dimensional form and derive the relevant dimensionless parameters. Section 3 discusses the computational approach and provides information on its validation. Results for miscible two-phase flows in capillary tubes are presented in §4, while the two-dimensional plane channel case is treated separately in an Appendix. We will place particular emphasis on the distinctly different dynamics observed for large and small Péclet number situations. Both of these regimes are analysed in detail, and we discuss their relationships with both the immiscible experiments of Taylor (1961) and Cox (1962), and the investigation of the dispersion of a passive scalar by Taylor (1953). While the simulations of §4 employ a constant molecular diffusion coefficient, the experimental observations in Part 1 suggest a strong dependence of this coefficient on the concentration. Section 5 presents simulation results for this case. Section 6 investigates the importance of the above-mentioned Korteweg stresses, as well as of the divergence of the velocity field. Finally, a brief summary as well as some conclusions are provided in §7.

2. Governing equations

We address the problem of the slow displacement, in an axisymmetric tube or a plane channel, of a fluid with dynamic viscosity μ_2 by a second fluid with a viscosity of μ_1. The numerical simulations to be discussed in the following are to complement

the experiments described in the companion paper, Part 1. Since in those experiments the Reynolds number Re consistently is $O(1)$ or less, we can neglect the influence of nonlinear inertial terms on the balance of momentum and base our analysis on the equations governing incompressible Stokes flow. The conservation of species gives rise to an additional convection–diffusion equation for the relative concentration c of fluid 2. We adopt the standard set of equations commonly employed to simulate incompressible miscible two-phase flows

$$\nabla \cdot \boldsymbol{u} = 0, \tag{2.1}$$

$$\nabla p = \nabla(\mu \nabla)\boldsymbol{u} + \rho g \boldsymbol{e}_g, \tag{2.2}$$

$$\frac{\partial c}{\partial t} + \boldsymbol{u} \cdot \nabla c = D \nabla^2 c. \tag{2.3}$$

Here $\boldsymbol{u} = (u, v)$ denotes the fluid velocity vector, p pressure, and t time, while μ and ρ indicate the dynamic viscosity and density, respectively. Gravity has the magnitude g and points in the direction of the unit vector $\boldsymbol{e}_g$, which is assumed to be either parallel or antiparallel to the main flow direction, so that symmetry around the centreline can be assumed. In the first part of the investigation, the diffusion coefficient D is taken to be constant, which represents a considerable simplification, as the experimental measurements of Part 1 demonstrate its dependence on the concentration. Consequently, in §5 we will explore the influence of a variable diffusion coefficient. Both density and viscosity are assumed to be functions of concentration only

$$\rho = \rho(c), \qquad \mu = \mu(c).$$

Recently, several researchers, most notably Joseph and coworkers, have drawn renewed attention to the fact that the above system of equations represents an approximation, and to the potential role played by additional stresses in miscible flows, an issue already discussed by Korteweg (1901). Joseph & Renardy (1993) provide an extensive discussion of the relevant physical issues and their proper mathematical modelling. As was already pointed out by Joseph (1990), there are two separate effects of potential importance. Firstly, if the density of the mixture of miscible fluids depends on the concentration, the velocity field is no longer divergence free, even though the fluid is incompressible. This can be seen immediately from the continuity equation, which reads

$$\frac{\mathrm{d}\rho}{\mathrm{d}t} = -\rho \nabla \cdot \boldsymbol{u} \tag{2.4}$$

where

$$\frac{\mathrm{d}}{\mathrm{d}t} = \frac{\partial}{\partial t} + \boldsymbol{u} \cdot \nabla. \tag{2.5}$$

As the density of a fluid element changes continuously due to diffusion, the divergence of the velocity field does not vanish, thereby giving rise to an additional stress tensor in the momentum equation. Joseph & Hu (1991) find that, under certain conditions, these stresses can act in a fashion similar to surface tension in the region of contact between two miscible liquids. Since the magnitude of these stresses depends on some (unknown) material properties of the mixture, it is difficult to provide values for their absolute magnitude. However, in §6 we will present scaling arguments that allow us to estimate their importance for the type of flow field considered in the present investigation.

The second source of additional stresses in miscible liquids discussed by Joseph & Hu (1991) originates in the different chemical potentials of the two liquids, cf. also Davis (1988). Again, an unknown material quantity renders an estimation of

their magnitude difficult, but scaling arguments can provide some limited information, cf. §6.

At the wall, we have the conventional boundary conditions of no normal flow and no slip, as well as vanishing normal derivatives of the concentration field. Since our interest lies mostly in the long-time asymptotic nature of the velocity and concentration fields far away from the tube ends, as opposed to the detailed flow features near the inlet and outlet, we consider the situation of a pipe or channel whose upstream half initially only contains fluid 1, while the downstream half is filled with fluid 2. For all times then, far upstream of the mixing region only fluid 1 will be present, while far downstream there will be pure fluid 2. In these regions, the velocity profile asymptotically approaches that of Poiseuille flow. We assume furthermore that the volumetric flow rate does not change with time. This is slightly different from the experimental situation, in which a constant pressure drop over the length of the tube leads to an increase in volume flux with time, as a result of the decreasing overall effective viscosity. However, this change in the flow rate occurs very slowly, so that the experimental results can be considered quasi-steady. For a capillary tube of diameter d, with the streamwise and radial directions denoted by x and r, respectively, the boundary conditions thus are

$$r = 0: \qquad \frac{\partial u}{\partial r} = 0, \qquad v = 0, \qquad \frac{\partial c}{\partial r} = 0; \tag{2.6}$$

$$r = \frac{d}{2}: \qquad u = 0, \qquad v = 0, \qquad \frac{\partial c}{\partial r} = 0; \tag{2.7}$$

$$x \to -\infty: \qquad u(r) = U\left(1 - \frac{4r^2}{d^2}\right), \qquad c(r) = 0; \tag{2.8}$$

$$x \to \infty: \qquad u(r) = U\left(1 - \frac{4r^2}{d^2}\right), \qquad c(r) = 1. \tag{2.9}$$

Here, U denotes the value of the Poiseuille flow velocity profile at the centreline, while u and v are the axial and radial velocity components, respectively. For the plane channel, the boundary conditions take the corresponding two-dimensional form. In order to render the above equations and boundary conditions dimensionless, we refer all velocities to U and all lengths to d. A characteristic pressure is provided by $\mu_2 U/d$, and all densities and viscosities are referred to $\rho_1 - \rho_2$ and μ_2, respectively. Consequently, the equations for the non-dimenensional variables take the form

$$\nabla \cdot \boldsymbol{u} = 0, \tag{2.10}$$

$$\nabla p = \nabla(\mu \nabla)\boldsymbol{u} + F\rho \boldsymbol{e}_g, \tag{2.11}$$

$$\frac{\partial c}{\partial t} + \boldsymbol{u} \cdot \nabla c = \frac{1}{Pe} \nabla^2 c \tag{2.12}$$

with the boundary conditions

$$r = 0: \qquad \frac{\partial u}{\partial r} = 0, \qquad v = 0, \qquad \frac{\partial c}{\partial r} = 0; \tag{2.13}$$

$$r = 0.5: \qquad u = 0, \qquad v = 0, \qquad \frac{\partial c}{\partial r} = 0; \tag{2.14}$$

$$x \to -\infty: \qquad u(r) = 1 - 4r^2, \qquad c(r) = 0; \tag{2.15}$$

$$x \to \infty: \qquad u(r) = 1 - 4r^2, \qquad c(r) = 1. \tag{2.16}$$

As the governing dimensionless parameters we identify a Péclet and a gravity number.

In addition, the fluid properties provide a dimensionless viscosity ratio in the form of an Atwood number

$$Pe = \frac{Ud}{D}, \qquad F = \frac{gd^2}{v_2 U}\frac{\rho_1 - \rho_2}{\rho_2}, \qquad At = \frac{\mu_2 - \mu_1}{\mu_2 + \mu_1}. \tag{2.17}$$

Notice that the above dimensionless parameters are formed with the centreline velocity of the Poiseuille flow profile. It should furthermore be pointed out that the above approach implies that the Schmidt number

$$Sc = \frac{v}{D} \tag{2.18}$$

tends to infinity, as we consider convective effects to be of importance in the species conservation equation, but not in the momentum equation. In order to obtain a closed system of equations and boundary conditions, it remains to specify how the viscosity and density depend on the concentration. For most fluid mixtures, a linear density–concentration relationship represents a good approximation, so that we can write for the dimensionless density

$$\rho = \frac{\rho_1}{\rho_2 - \rho_1} + c. \tag{2.19}$$

For the dependence of the dimensionless viscosity on the concentration we follow other authors (e.g. Tan & Homsy 1986; Rogerson & Meiburg 1993*a*,*b*) by specifying an exponential relationship

$$\mu = \mathrm{e}^{R(c-1)}, \qquad R = \ln\left(\frac{\mu_2}{\mu_1}\right). \tag{2.20}$$

Here, R is related to At by

$$At = \frac{\mathrm{e}^R - 1}{\mathrm{e}^R + 1}. \tag{2.21}$$

Notice, however, that for the water–glycerine system employed in Part 1, the (μ,c)-relationship is closer to a doubly exponential function for glycerine concentrations above 20%. The possible importance of this point will be discussed further below.

3. Computational approach

Since we assume symmetry about the centreline of the tube or channel, it will be advantageous to express the governing equations and boundary conditions in terms of a streamfunction formulation. In this way, the pressure variable is eliminated, and the continuity equation is satisfied identically. For axisymmetric flow, we obtain the following relationships between the scalar streamfunction ψ and the velocity components:

$$u = \frac{1}{r}\frac{\partial \psi}{\partial r}, \qquad v = -\frac{1}{r}\frac{\partial \psi}{\partial x}. \tag{3.1}$$

By cross-differentiating and combining the two components of the momentum equation, we obtain for the streamfunction

$$\nabla^4 \psi = -\mathrm{g}(x,r) + \frac{F}{\mu} r \frac{\partial c}{\partial r}, \tag{3.2}$$

where

$$\nabla^4 = \frac{\partial^4}{\partial r^4} + 2\frac{\partial^4}{\partial r^2 \partial x^2} + \frac{\partial^4}{\partial x^4},$$

$$\begin{aligned} g = {} & 2\left(R\frac{\partial c}{\partial r} - \frac{1}{r}\right)\frac{\partial^3 \psi}{\partial r^3} + 2R\frac{\partial c}{\partial x}\frac{\partial^3 \psi}{\partial x^3} - 2\left(\frac{1}{r} - R\frac{\partial c}{\partial r}\right)\frac{\partial^3 \psi}{\partial r \partial x^2} + 2R\frac{\partial c}{\partial x}\frac{\partial^3 \psi}{\partial r^2 \partial x} \\ & + \left[R\frac{\partial^2 c}{\partial r^2} + R^2\left(\frac{\partial c}{\partial r}\right)^2 - R\frac{\partial^2 c}{\partial x^2} - R^2\left(\frac{\partial c}{\partial x}\right)^2 - R\frac{3}{r}\frac{\partial c}{\partial r} + \frac{3}{r^2}\right]\frac{\partial^2 \psi}{\partial r^2} \\ & + \left[R\frac{\partial^2 c}{\partial x^2} + R^2\left(\frac{\partial c}{\partial x}\right)^2 - R\frac{\partial^2 c}{\partial r^2} - R^2\left(\frac{\partial c}{\partial r}\right)^2 - R\frac{1}{r}\frac{\partial c}{\partial r}\right]\frac{\partial^2 \psi}{\partial x^2} \\ & + 2\left[2\left(R\frac{\partial^2 c}{\partial r \partial x} + R^2\frac{\partial c}{\partial r}\frac{\partial c}{\partial x}\right) - R\frac{1}{r}\frac{\partial c}{\partial x}\right]\frac{\partial^2 \psi}{\partial r \partial x} \\ & + \left[R\frac{3}{r^2}\frac{\partial c}{\partial r} - \frac{1}{r}\left(R\frac{\partial^2 c}{\partial r^2} + R^2\left(\frac{\partial c}{\partial r}\right)^2\right) + \frac{1}{r}\left(R\frac{\partial^2 c}{\partial x^2} + R^2\left(\frac{\partial c}{\partial x}\right)^2\right) - \frac{3}{r^2}\right]\frac{\partial \psi}{\partial r} \\ & - \frac{2}{r}\left(R\frac{\partial^2 c}{\partial r \partial x} + R^2\frac{\partial c}{\partial r}\frac{\partial c}{\partial x}\right)\frac{\partial \psi}{\partial x}. \end{aligned}$$

For the species conservation equation, we obtain

$$\frac{\partial c}{\partial t} + \frac{1}{r}\frac{\partial \psi}{\partial r}\frac{\partial c}{\partial x} - \frac{1}{r}\frac{\partial \psi}{\partial x}\frac{\partial c}{\partial r} = \frac{1}{Pe}\left(\frac{1}{r}\frac{\partial}{\partial r}\left(r\frac{\partial c}{\partial r}\right) + \frac{\partial^2 c}{\partial x^2}\right). \tag{3.3}$$

Again, for the plane channel flow, the above relationships take their corresponding forms in Cartesian coordinates. Boundary conditions for ψ have to be specified such that both the wall and the centreline are streamlines. We arbitrarily set the value of the streamfunction at the centreline to zero. By requiring its wall value to be 0.125, we ensure that the volume flux through the tube is equal to that of Poiseuille flow with unit centreline velocity. Furthermore, the no-slip condition at the wall causes the wall-normal derivative of ψ at the wall to vanish. At the centreline, the symmetry condition for the streamwise velocity component results in

$$\frac{\partial}{\partial r}\left(\frac{1}{r}\frac{\partial \psi}{\partial r}\right) = 0 \tag{3.4}$$

so that we obtain the condition that the derivative of the streamfunction in the direction normal to the centreline has to vanish as well. Consequently, the set of boundary conditions for ψ takes the form

$$r = 0: \quad \psi = 0, \quad \frac{\partial \psi}{\partial r} = 0, \quad \frac{\partial c}{\partial r} = 0; \tag{3.5}$$

$$r = 0.5: \quad \psi = 0.125, \quad \frac{\partial \psi}{\partial r} = 0, \quad \frac{\partial c}{\partial r} = 0. \tag{3.6}$$

For reasons of computational efficiency, most of our simulations will employ a control volume that is moving in the direction of the flow with a possibly time-dependent velocity V approximately equal to the propagation speed of the advancing concentration front. The use of such a moving control volume allows us to take the simulation to long times without having to discretize large regions of nearly unperturbed Poiseuille flow. In the reference frame of this moving control volume, the fluid velocity at the wall becomes $-V$, so that there the boundary condition on

the normal derivative of the streamfunction changes to

$$\frac{\partial \psi}{\partial r} = -0.5V. \tag{3.7}$$

For simplicity, from now on x will refer to the streamwise coordinate in this moving reference frame. In terms of this coordinate, the moving computational control volume typically extends from the inflow boundary, located a short distance upstream of the advancing front at $x = 0$, to the outflow boundary, which is located downstream of the front at $x = L$. Depending on the particular flow conditions, both the upstream and the downstream borders can become mixed inflow/outflow boundaries. The boundary conditions to be specified at these locations have to be able to handle such situations without causing any disturbances to propagate into the interior of the computational domain. In the present investigation, we impose the boundary conditions of a vanishing second streamwise derivative for the concentration, and vanishing second and fourth derivatives for the streamfunction

$$x = 0, \quad L: \qquad \frac{\partial^2 c}{\partial x^2} = 0, \qquad \frac{\partial^2 \psi}{\partial x^2} = 0, \qquad \frac{\partial^4 \psi}{\partial x^4} = 0. \tag{3.8}$$

Here, the last condition corresponds to a vanishing second derivative of the vorticity in the more traditional streamfunction–vorticity formulation. Test results to be presented in the next section will demonstrate the appropriateness of these boundary conditions.

The above system of partial differential equations (2.12), (3.2), subject to the boundary conditions (3.5), (3.6), (3.8) is integrated numerically by combining an ADI scheme (Fletcher 1988) for the concentration equation with a multigrid approach (Brandt 1977) for the elliptic streamfunction equation. At time $t = 0$, a one-dimensional concentration field in the form of an error function is specified, along with a Poiseuille flow velocity profile throughout the entire length of the tube. Subsequently, the concentration equation is used to advance the calculation in discrete time steps. The velocity field is evaluated from the streamfunction equation at every intermediate and full time step. The formulation of computational boundary conditions at the intermediate time step levels poses no problems due to the nature of the mathematical boundary conditions.

The concentration equation is discretized by means of four-point, third-order upwind stencils for the convective terms (Fletcher 1988)

$$u \geqslant 0: \frac{\partial c}{\partial x} = \frac{c_{i+1} - c_{i-1}}{2\Delta x} + \frac{c_{i-2} - 3c_{i-1} + 3c_i - c_{i+1}}{6\Delta x}, \tag{3.9}$$

$$u < 0: \frac{\partial c}{\partial x} = \frac{c_{i+1} - c_{i-1}}{2\Delta x} + \frac{c_{i-1} - 3c_i + 3c_{i+1} - c_{i+2}}{6\Delta x}, \tag{3.10}$$

with corresponding expressions in the radial direction. The diffusive terms are represented by five-point, fourth-order central stencils. At all boundaries, both the convective and the diffusive terms are discretized by second-order central stencils. The streamfunction equation is discretized by second-order central stencils as well.

3.1. *Validation*

A few obvious and somewhat trivial test cases concern the one-dimensional self-similar diffusion of the initial concentration profile in the absence of flow, and the reproduction of Poiseuille flow throughout the tube for the case of equal viscosities. In addition, we carried out validation studies for different grid spacings and time steps in order to establish appropriate discretization levels as a function of Pe, and

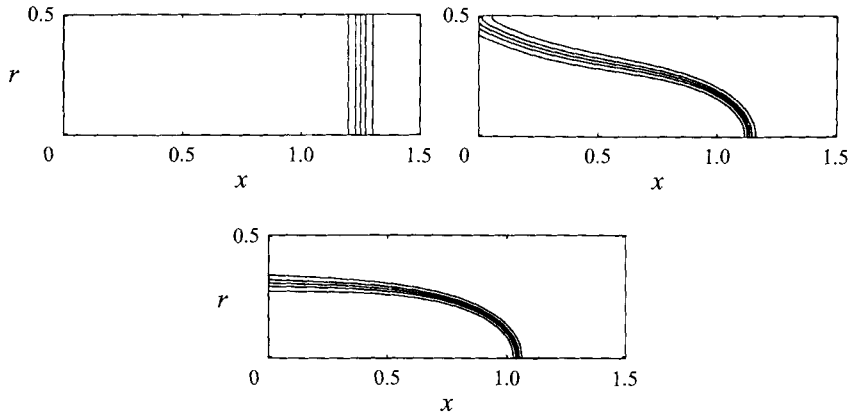

FIGURE 1. Concentration contours at times 0, 1, and 3 for $R = 5$, $F = 0$, and $Pe = 1600$. Notice the formation of an axisymmetric finger with a steep concentration front at its tip.

to test the convergence properties of the computational procedures. Such calculations demonstrated that quantities of interest, such as the finger propagation velocity, have converged to within less than 1% for $Pe\Delta x = 6.25$, which hence serves as our criterion for selecting the grid spacing, taken to be equal in both directions, as a function of Pe. To advance the calculation in time, we apply a constant time step $\Delta t = 0.005$, which was established by means of test calculations. Finally, we simulated identical physical situations with computational domains of different sizes, in order to establish the validity of the inflow and outflow boundary conditions. The results of these test calculations, some of which will be described in more detail below, demonstrated the stablity and convergence of the computational approach. The comparison with the experimental data of Part 1 in itself of course represents a further check of the numerical results, as do scaling laws to be presented below.

4. Results

4.1. $Pe \geqslant O(10^3)$

The evolution of the flow in this parameter regime is exemplified by the case $Pe = 1600$ and $R = 5$ ($At = 0.9866$), shown in figure 1 in the moving reference frame. The levels of the plotted concentration contours are $c = 0.1, 0.3, \ldots, 0.9$. Gravity is absent for this flow, i.e. $F = 0$. As described above, the initial condition specifies a one-dimensional error-function profile for the concentration, along with axisymmetric Poiseuille flow for the velocity components. The velocity field immediately results in a strong deformation of the concentration distribution in the interior of the tube, while at the wall concentration changes are the result of diffusion only. The transient evolution of the concentration distribution, in turn, causes corresponding changes in the viscosity field, thereby modifying the velocity field. This effect distinguishes the present situation from the one analysed by Taylor (1953), in which there is no feedback by the concentration distribution onto the velocity field. For the present parameters, we observe the development of a well-defined finger of the less-viscous fluid in the centre of the tube. The finger tip consists of a steep concentration front, while its sides are formed by diffusively spreading concentration layers. In order to test the validity of the computational inflow and outflow boundary conditions, the same physical situation was simulated in a larger control domain, cf. figure 2.

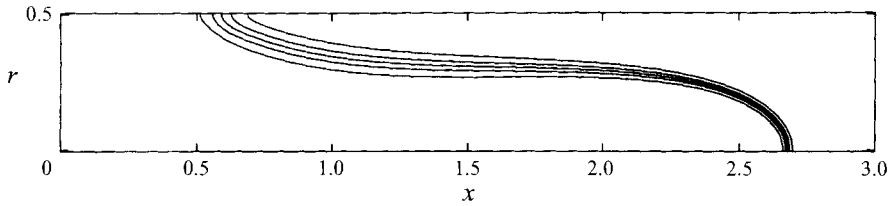

FIGURE 2. The same flow as in figure 1, simulated in a larger computational domain, at $t = 1.75$. The concentration contours for the two different computational domain sizes are virtually identical, indicating that both the numerical inflow and outflow boundary conditions as well as the domain size do not affect the solution.

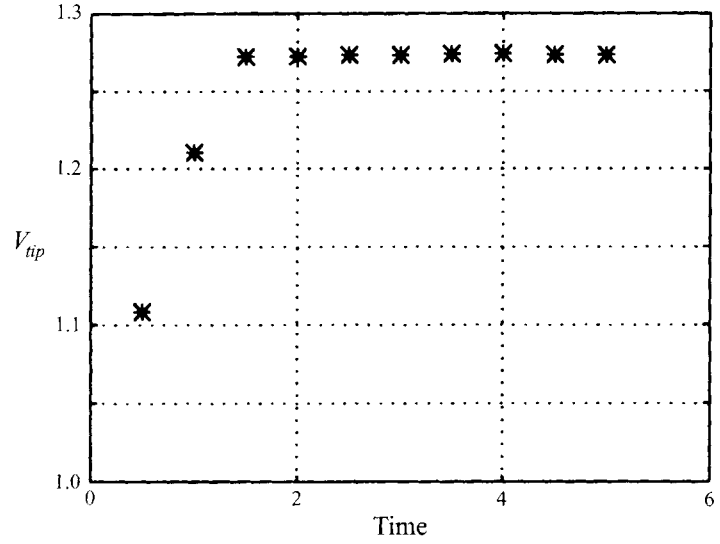

FIGURE 3. The finger tip velocity, defined as the propagation velocity of the $c = 0.5$ contour, as a function of time for $R = 5$, $F = 0$, and $Pe = 1600$. Both the tip velocity and the concentration contours indicate the emergence of a quasi-steady state for the present parameters.

When plotted in the same figure, the contours of the two simulations are virtually indistinguishable, which indicates that the mixed inflow/outflow boundary at $x = 0$ is handled well by the present set of numerical boundary conditions, as there are no detectable disturbances propagating from the boundary into the computational domain. The comparison further establishes that the smaller computational domain yields the correct finger tip velocity V_{tip} and film thickness.

By the time $t = 2$, the finger tip shape and the associated concentration field have reached a quasi-steady state, in the reference frame moving with the finger tip. This is confirmed by figure 3, which depicts the propagation velocity of the finger tip as a function of time. Unless otherwise stated, from here on the tip velocity is defined as the velocity with which the $c = 0.5$ contour propagates along the tube's axis. Note that the propagation velocity of the contour is smaller than the instantaneous fluid velocity at its location, due to the effect of diffusion. This effect diminishes with increasing Pe. The accompanying streamline pattern in the reference frame moving with the tip velocity (figure 4) shows the existence of a stagnation point at the tip, along with an associated strain field, as predicted by Taylor (1961) for the case of an immiscible two-phase flow in which over half of the displaced fluid is left behind on

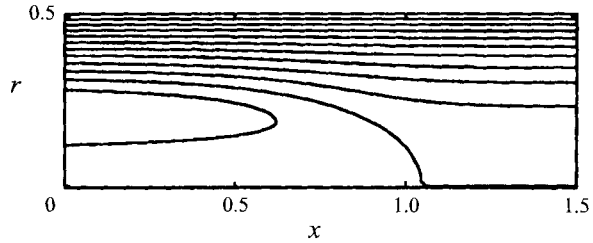

FIGURE 4. The streamline pattern in the reference frame moving with the finger tip velocity, for $R = 5$, $F = 0$, and $Pe = 1600$ at $t = 3$. Since the propagation velocity is larger than the centreline velocity of the Poiseuille flow, the tip region has the character of a stagnation point flow field. Compression in the axial direction balances the effects of diffusion in maintaining a steep concentration front.

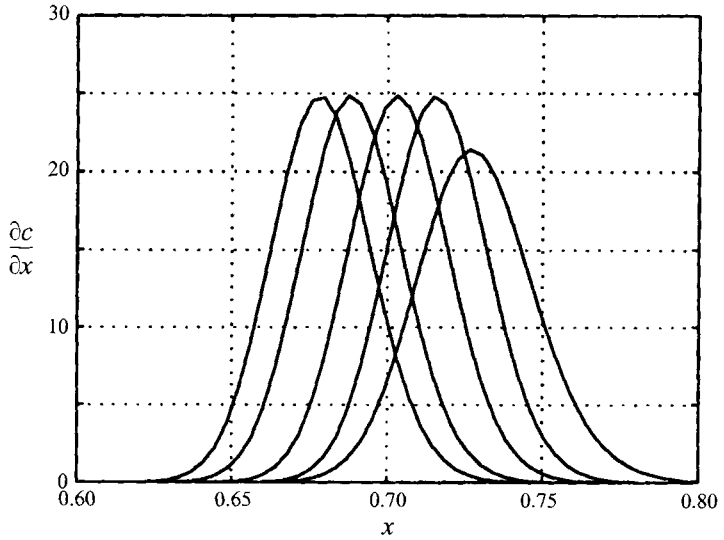

FIGURE 5. $\partial c/\partial x(r = 0)$ for $R = 5$, $F = 0$, and $Pe = 1600$. From right to left, the curves correspond to times 1, 2, 3, 4, and 5, respectively. The shift of the contours with time is a result of the moving reference frame. These concentration derivative profiles confirm the existence of the quasi-steady state.

the tube wall. For this case of immiscible displacement, the streamline pattern near the finger tip is steady in the moving reference frame, and the streamline originating from the stagnation point denotes the interface between the two fluids. For the present, miscible flow this separatrix still tracks the concentration layer; however, due to diffusion, *both* fluids are present on both sides of it. The concentration derivative along the centreline $\partial c/\partial x(x, r = 0)$ demonstrates the emergence of a quasi-steady state as well (figure 5). Notice that, due to the moving reference frame, the location of the maximum concentration derivative moves to smaller x with increasing time. This figure quantifies the steepness of the concentration front at the finger tip, which is determined by the local balance of strain and diffusion. An estimate for the strength α of the local strain field can be obtained by realizing that it is determined by the difference of the streamwise velocities ahead of and behind the finger tip. This velocity difference of approximately $2(V_{tip} - U)$ is achieved over a distance comparable to the

tube radius, so that we obtain

$$\alpha \approx \frac{4(V_{tip} - U)}{d}. \tag{4.1}$$

Notice that here, as well as in the following, scaling arguments are usually given in terms of *dimensional* quantities. A straightforward one-dimensional balance of strain and diffusion effects on the concentration field according to

$$u\frac{\partial c}{\partial x} = D\frac{\partial^2 c}{\partial x^2} \tag{4.2}$$

then yields for the front thickness δ_0 at the finger tip

$$\frac{\delta_0}{d} \approx \left(\frac{D}{2(V_{tip} - U)d}\right)^{1/2} \tag{4.3}$$

which indicates that the front thickness scales with the square root of the inverse of a modified Péclet number formed with the velocity difference across the finger tip. For the present case, this yields $\delta_0/d \approx 1/30$, which is in good agreement with figure 5. The one-dimensional analysis furthermore gives

$$\left.\frac{\partial c}{\partial x}\right|_{max} \approx \left(\frac{2}{\pi}\frac{(V_{tip} - U)d}{D}\right)^{1/2} \tag{4.4}$$

which for the present parameters yields approximately 17. Considering the rough estimate of the strain intensity, along with the one-dimensional simplification of the balance argument, the agreement with the computational results of figure 5 is reasonable, confirming that the concentration field near the finger tip is indeed determined by a nearly one-dimensional balance of strain and diffusion.

On the sides of the finger, the concentration layers grow diffusively with increasing distance from the finger tip, cf. figures 1 and 2. These layers will merge when their local thickness becomes comparable to the tube radius, i.e. when $\delta/d \approx 0.5$. Straightforward scaling yields

$$\frac{\delta}{d} \approx \left(\frac{Dt}{d^2}\right)^{1/2} \tag{4.5}$$

Here t is the time period over which the concentration layer has spread diffusively. This layer is thickest near the root of the finger, where it has been diffusing for a time that can be estimated by the finger's instantaneous length L_f and its tip velocity V_{tip}:

$$t \approx \frac{L_f}{V_{tip}}. \tag{4.6}$$

Consequently, the diffusion layers will merge at the root of the finger, once it has reached a length

$$\frac{L_f}{d} \approx \frac{Pe}{4}. \tag{4.7}$$

Subsequently, the supply of uncontaminated fluid to the tip region will gradually be cut off, and eventually the quasi-steady state will begin to decay. The above scaling laws indicate that we can neither employ a sufficiently large computational domain, nor can we carry the simulation to times that are sufficiently long to capture these effects for the present set of parameters.

For practical considerations, a relevant quantity is the fraction of more-viscous

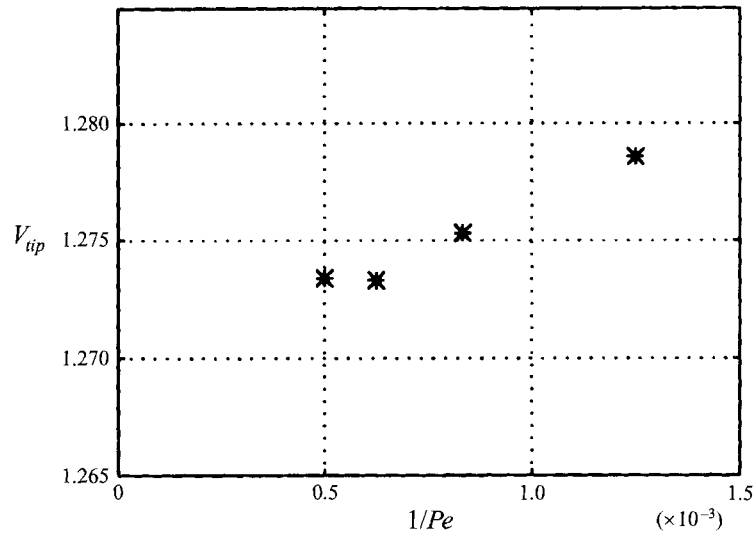

FIGURE 6. The quasi-steady finger tip velocity as a function of $1/Pe$ for $R = 5$ and $F = 0$. The figure indicates that for $Pe = 1600$ the finger velocity is within less than 1% of the extrapolated value for $Pe \to \infty$.

fluid left behind on the walls of the tube once the quasi-steady state has developed. For immiscible flow, Taylor (1961) calculates this fraction (an effective 'film thickness' of the fluid) from the finger tip velocity as

$$m = 1 - \frac{U}{2V_{tip}}. \tag{4.8}$$

The same relationship is employed in Part 1 in order to determine the fraction of fluid left behind on the tube wall for the present case of miscible displacement. In particular, it is of interest to record $m = m(At)$ in the limit of infinitely large Pe. Since grid-based numerical simulations will not provide accurate results for this limit, we resort to an extrapolation procedure for $V_{tip} = f(Pe^{-1})$, cf. figure 6. As mentioned above, we keep $Pe\Delta x$ constant in all calculations, so that numerical parameters have only a minimal effect on the variation of the tip velocity observed in figure 6. However, small inaccuracies in the evaluation of the tip velocity may be caused by the interpolation procedure used to determine the instantaneous location of the $c = 0.5$ contour. Still, it is clear that the tip velocity for $Pe = 1600$ is within less than 1% of the extrapolated value for $Pe \to \infty$. In view of the considerable computational cost associated with carrying out several simulations at different large Pe for each value of R in order to perform the extrapolation, we will in the following present the simulation results for $Pe = 1600$ in lieu of $Pe \to \infty$. In this way, we arrive at the (m, At)-relationship depicted in figure 7. It needs to be pointed out that only the data for $At \geqslant 0.75$ correspond to truly quasi-steady states for $Pe = 1600$. Those calculations yielded concentration fields and propagation velocities of the $c = 0.5$ contour that stayed constant for at least some time, cf. the discussion below. For $R = 1$ ($At = 0.462$), such a quasi-steady state was never fully reached, although for some length of time the propagation velocity varied quite slowly. This nearly constant tip velocity gives $m < 0.5$, at least partially due to finite-Pe effects, which lead to a diffusive slowing of the finger tip, and thereby to a reduced film thickness. For

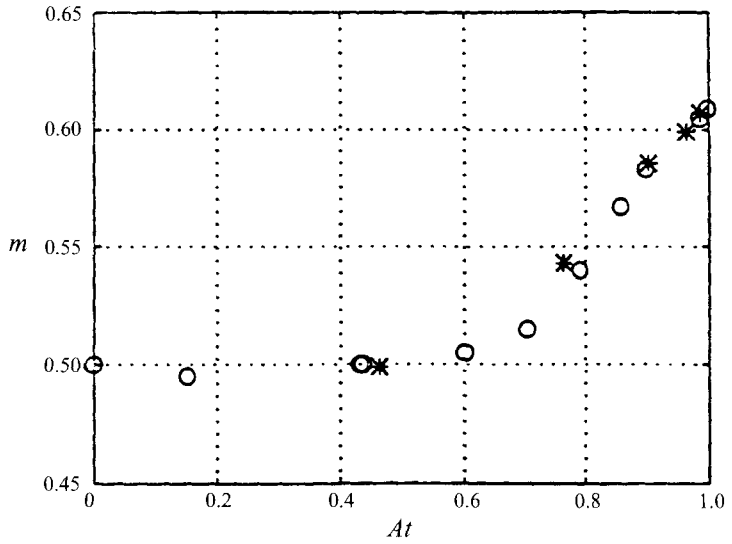

FIGURE 7. Fraction of the displaced fluid left behind on the tube wall, as a function of the viscosity ratio, for large Pe and $F = 0$: *, present numerical results; o, experimental values from Part 1. The limiting value of $m \approx 0.61$ for $At \to 1$ is in good agreement with the observations by Cox (1962) for immiscible flow with $At \to 1$ and $Ca \to \infty$.

comparison, the experimental values from Part 1 are shown as well. The agreement is resonable, although not perfect. Some of the possible reasons for the observed discrepancy, such as a variable diffusion coefficient or the influence of additional stresses which are not accounted for in the simulations, will be discussed below. Furthermore, there may be some small non-axisymmetric effects in the experiments, due to density differences between the two phases, cf. the discussion in Part 1. Finally, as pointed out above, the (μ, c)-relationship of the fluids used in the experiments is somewhat different from that employed in the simulations.

It should be mentioned that Yang & Yortsos (1996), based on the asymptotic *transverse flow equilibrium (TFE) concept*, find a quantitatively somewhat different dependence of the film thickness on the viscosity ratio, especially at high values of At. A careful evaluation of the assumptions underlying the TFE concept by these authors shows that they become less accurate in regions of steep transverse fronts, i.e. near the finger tip at large values of Pe. In this context, it is important to appreciate the crucial rule played by the finger tip in setting the overall width of the finger. As, for example, the early asymptotic work by Bretherton (1961) and the nonlinear calculations by Reinelt & Saffman (1985) show, the film thickness is completely determined by the flow in this region, where the TFE approach is least accurate, which explains the observed discrepancy. The finger shape obtained in the lattice gas simulations by Rakotomalala, Salin, & Watzky (1996), on the other hand, suggests good qualitative agreement with the present simulatons.

It is interesting to note that the value $m \approx 0.61$ for the film thickness in the limit $At \to 1$, $Pe \to \infty$ agrees well with the observations by Cox (1962) for immiscible flow in the limit $At \to 1$, $Ca \to \infty$, where Ca denotes the capillary number. This indicates that as diffusion or surface tension, respectively, become very small, their dynamical significance decays to zero in a smooth fashion, so that the shape of the finger tip is determined by the viscosity contrast alone.

It should be emphasized that the above results apply to the *quasi-steady* state that will develop for certain parameters and persist for a finite time only. For finite values of Pe, this quasi-steady state eventually always decays. As will be discussed in more detail below, the concentration field then approaches the classical case of Taylor dispersion, so that the velocity of the $c = 0.5$ contour asymptotically decays to $V_{tip} = 0.5$, which, if substituted into equation (4.8), results in $m = 0$. This limiting value of m is appropriate from the point of view that for infinitely long times indeed all of fluid 2 will be expelled, due to the action of diffusion. However, in contrast to immiscible flows, a vanishing m does not indicate that there is no fluid 2 to be found upstream of the finger tip, defined in terms of the $c = 0.5$ contour. The above observations indicate the limited usefulness of defining the 'finger tip' location, as well as its velocity, in terms of the $c = 0.5$ contour. However, there is no obvious better definition of the finger tip for miscible displacements.

An important question concerns the parameter values for which the above quasi-steady state will be observed. As discussed above, strain and diffusion have to balance each other in such a way that a steep concentration front can be maintained. This quasi-one-dimensional balance can only exist if the front thickness at the tip, δ_0, is significantly smaller than the tube diameter d. Consequently, there will be an intermediate range of diffusion values over which a gradual transition takes place. Beyond this transitional range, the strain can no longer maintain a sufficiently steep front. In other words, a transitional Pe-regime exists, below which the strain field will not be strong enough to counter the tendency of diffusion to smear out the finger front. The condition $\delta_0/d < C_1$, with $C_1 \ll 1$, leads to an estimate for this transitional Pe-regime. With the above relationship (4.3) and $V_{tip} \approx 1.25U$ for $R = 5$, we obtain

$$\frac{\delta_0}{d} \approx \left(\frac{2}{Pe}\right)^{1/2} < C_1. \tag{4.9}$$

For $C_1 = 1/10$ and $1/20$, this criterion yields $Pe = 200$ and 800, respectively. Since the finger velocity, and consequently the strength of the strain field, depend on R, we expect the transitional Pe-range to vary with R as well. Figure 7 shows a reduced tip velocity for decreasing R, resulting in a weaker strain field. Consequently, the transitional Pe will increase for smaller values of R. Notice that in the limit of $R \to 0$ ($At \to 0$), not even $Pe \to \infty$ results in a quasi-steady concentration field at the finger tip, as the concentration contours are continuously being deformed by the Poiseuille flow profile, even though the propagation velocity of the $c = 0.5$ contour remains constant. Our numerical simulations for $R = 5$ show the development of a quasi-steady finger with a steep front for $Pe \geqslant 800$, and a diffusing finger tip for $Pe \leqslant 400$. These Pe-values are in reasonable agreement with the transitional range estimated above. For lower values of R, we obtain diffusing fingers even for $Pe = 800$, again in line with the predicted trend.

A comparison of figure 8 ($R = 1$, $At = 0.462$, $Pe = 1{,}600$ at $t = 7$) with figure 2 demonstrates the effect of the viscosity ratio on the finger tip shape. Unless otherwise noted, in all following plots of the concentration field the contour levels are 0.1, 0.2, ..., 1.0. For this smaller viscosity contrast, the finger tip is more pointed than before, so that the finger reaches its asymptotic width only much farther upstream of the tip. In addition, the concentration front at the tip is not nearly as steep as before, in spite of identical Pe values. The reason lies in the much weaker strain field near the finger tip, due to the fact that the tip velocity is very close to the centreline velocity of the Poiseuille flow.

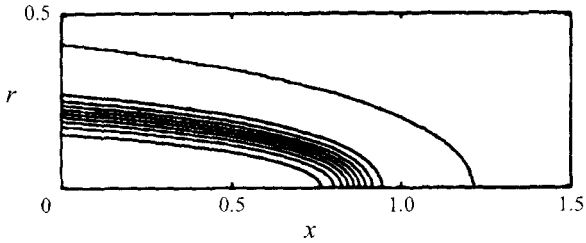

FIGURE 8. Concentration field for $R = 1$, $F = 0$, and $Pe = 1600$ at $t = 7$. The tip velocity is close to the centreline velocity of the Poiseuille flow. As a result, the weak related strain field cannot maintain a steep concentration front.

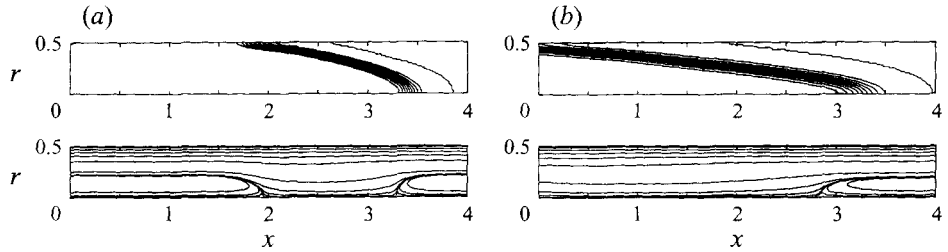

FIGURE 9. Concentration field (top) and streamline pattern (bottom) in moving reference frame for $R = -1$, $F = 0$, and $Pe = 1600$ at (*a*) $t = 2$ and (*b*) 5. Here a more-viscous fluid displaces a less-viscous one. The topology of the streamline pattern, as well as its effect on the evolving concentration field, are discussed in the text.

For the sake of completeness, we have also carried out simulations of cases in which a more-viscous fluid displaces a less-viscous one. For $R = -1$, $F = 0$, and $Pe = 1600$, figure 9 shows the concentration contours, as well as the streamline pattern in the reference frame moving with the instantaneous finger tip velocity, at times $t = 2$ and 5. The streamline pattern at $t = 2$ is topologically equivalent to the one depicted in figure 3(*c*) of Taylor's (1961) analysis of immiscible displacements. There is, however, an important distinction. While for Taylor's case the finger's surface is outlined by the streamline emanating from the upstream saddle, the finger in the present miscible displacement extends beyond the reverse flow region in the downstream direction. In the absence of diffusion, the downstream saddle would be found at the location where $c = 0.5$ on the centreline. However, since diffusion slows the contour down slightly, the saddle is displaced towards the inside of the finger tip. The fact that some of fluid 1 is located downstream of the saddle leads to a lengthening and thinning of the finger tip, since locally on the axis the u-velocity component is pointing away from the finger tip. As a result, there is no strain mechanism to balance diffusion, so that the concentration front at the finger tip becomes progressively smoother by time $t = 5$. The reverse flow region now extends beyond the upstream boundary of the computational domain. However, it is clear that a second saddle has to exist on the centreline somewhere upstream of the control volume, as Poiseuille flow is approached again, with a centreline velocity larger than that of the moving reference frame. Figure 10 confirms the above scenario. It displays the fluid velocity at the location of the $c = 0.5$ contour on the centreline, along with the velocities of the $c = 0.5$ and $c = 0.9$ contours themselves. The increasing distance between the $c = 0.5$ and $c = 0.9$ contours reflects the spreading concentration front.

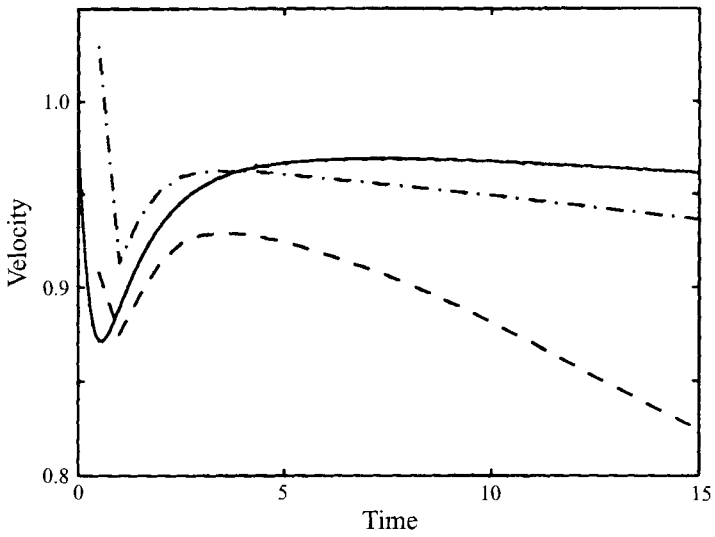

FIGURE 10. The fluid velocity (—) at the centreline location where $c = 0.5$, as well as the propagation velocities of the $c = 0.5$ (- - -) and $c = 0.9$ (- · - · -) contours, for the same parameters as in figure 9. It can be seen that a quasi-steady state does not develop. Furthermore, the different propagation velocities of the concentration contours indicate a progressive smoothing of the concentration field.

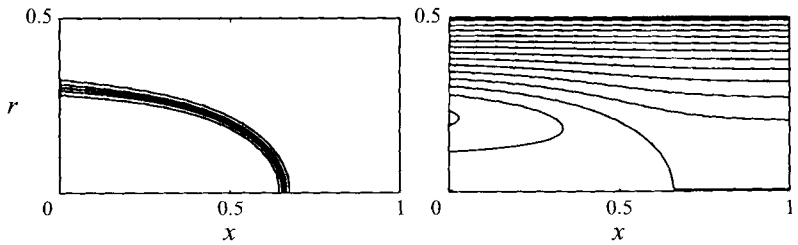

FIGURE 11. Concentration contours ($c = 0.1, 0.3, ..., 0.9$) and streamline pattern in the moving reference frame for $R = 5$, $F = 20.22$, and $Pe = 1600$ at time $t = 2.5$.

As a next step, we consider the effect of density differences in the presence of gravity on the flow. As mentioned before, the direction of gravity is aligned with the pipe, so that the axisymmetric nature of the flow is preserved. Positive values of the gravity parameter F correspond to the case of a denser fluid being displaced upwardly by a lighter fluid, or to lighter fluid being displaced by denser fluid in downward flow, with negative values of F indicating the opposite situation. In other words, for $F > 0$ the heavier fluid is always above the lighter one. Consequently, we expect the tip velocity to increase for $F > 0$, and to decrease for $F < 0$. Figure 11 demonstrates this influence for the case of $R = 5$, $F = 20.22$, and $Pe = 1600$, which again results in the formation of a quasi-steady state. The tip now moves faster than in the reference case without gravity (shown in figures 1 to 5), thereby generating a stronger strain field and a steeper concentration front, cf. figures 12 and 13. The streamline pattern in the reference frame moving with the $c = 0.5$ contour is topologically equivalent to that without gravity, cf. figure 4.

For negative values of F, the tip slows down compared to the no-gravity case. A weaker strain field results, so that, beyond a transitional range of gravity, a steep concentration front cannot be maintained, and a quasi-steady-state concentration

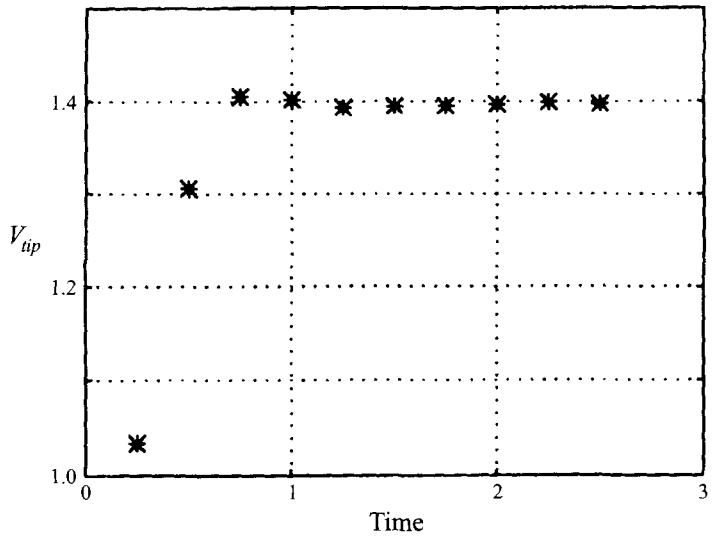

FIGURE 12. Finger tip velocity for the flow shown in figure 11. The unstable density stratification leads to a larger finger tip velocity, as well as a stronger related strain field, as compared to the case without gravity.

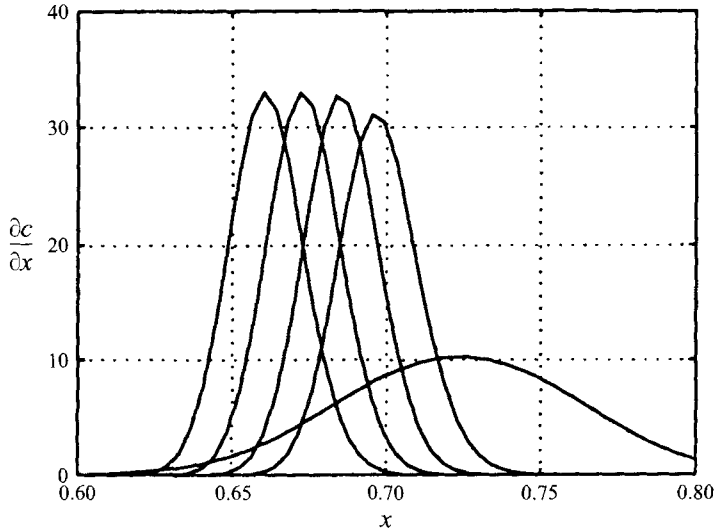

FIGURE 13. $\partial c/\partial x(r = 0)$ for $R = 5$, $F = 20.22$, and $Pe = 1600$. From right to left, the curves correspond to times 0.5, 1, 1.5, 2, and 2.5, respectively. The more intense strain results in a steeper concentration front at the finger tip.

field does not develop. In spite of this, the propagation velocity of the $c = 0.5$ contour nearly reaches a constant value, as shown in figure 14 for various combinations of R and F that all result in $V_{tip} < 1$. However, an overall more complex unsteady development takes place, as can be seen for $R = 2, F = -27.06$, and $Pe = 1600$. For these parameters, figure 15 shows the temporal evolution of the concentration field at times $t = 4$ and 10, along with the streamfunction at $t = 10$ in the reference frame moving with the $c = 0.5$ contour. The streamfunction field now exhibits a

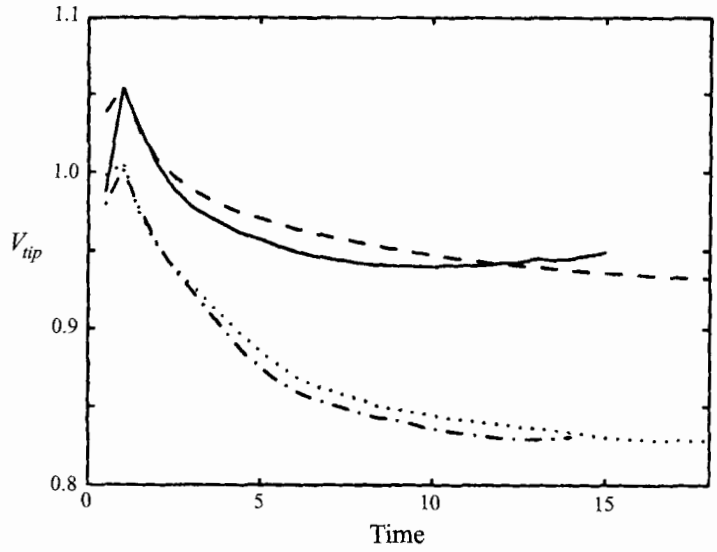

FIGURE 14. Propagation velocity of the $c = 0.5$ contour as a function of time for: $R = 2$, $F = -27.06$ (- - -); $R = 3$, $F = -49.8$ (· · ·); $R = 4$, $F = -54.94$ (- · - · -); $R = 5$, $F = -47.16$ (—).

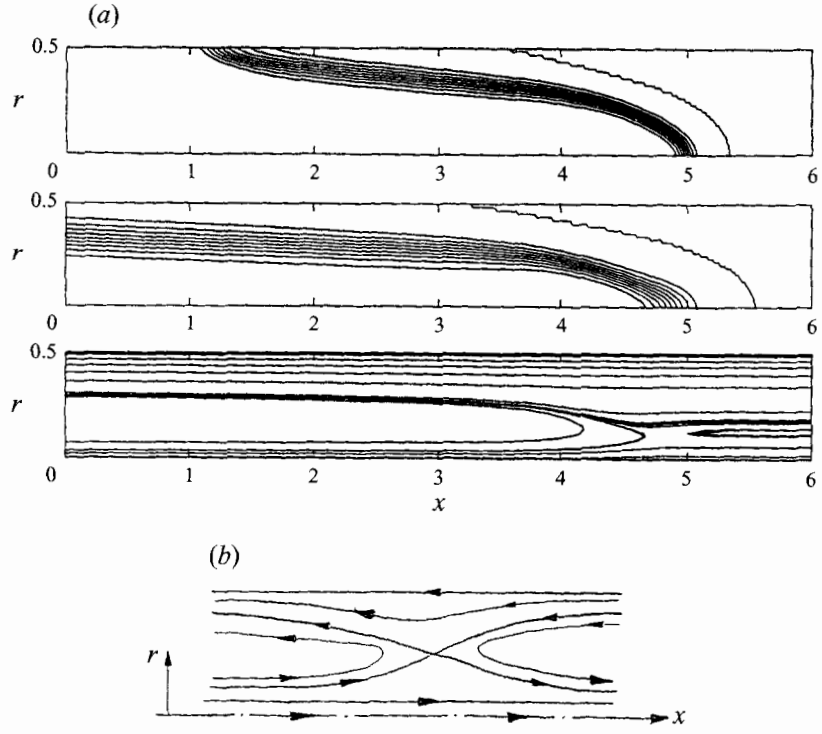

FIGURE 15. (*a*) Unsteady evolution of the concentration field for $R = 2$, $F = -27.06$, and $Pe = 1600$ at times $t = 4$ and 10, as well as the streamfunction in the reference frame moving with the $c = 0.5$ contour. (*b*) Sketch of the topological nature of the streamline pattern. Notice the off-axis saddle point. There is no reverse-flow region along the axis, so that fluid 1 is ejected in the downstream direction from the finger tip.

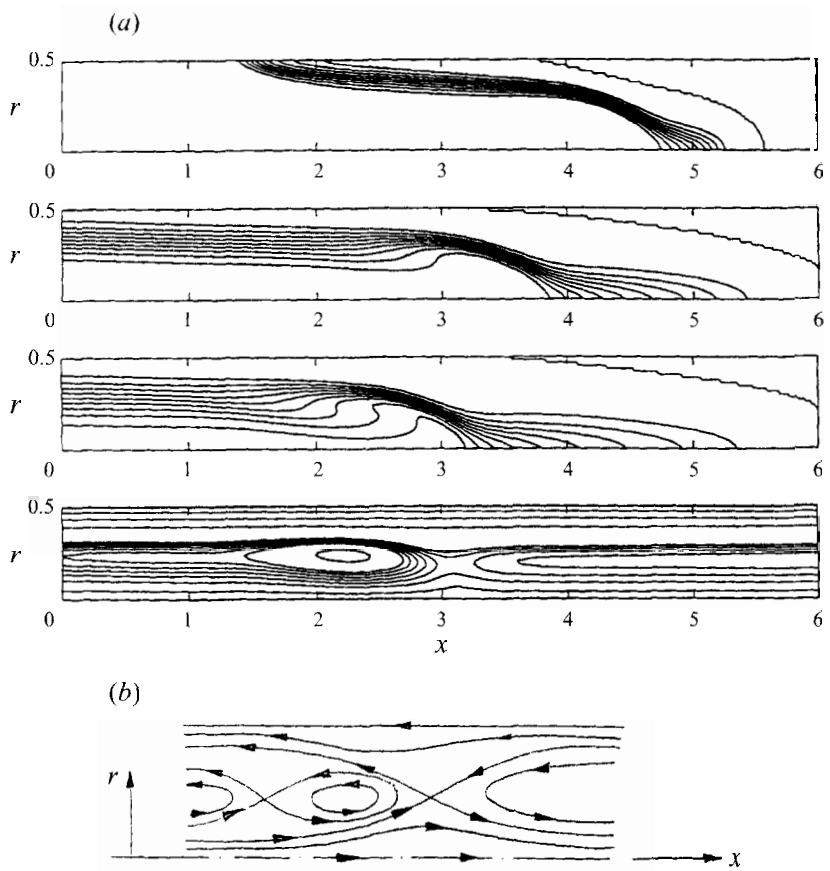

FIGURE 16. (*a*) Unsteady evolution of the concentration field for $R = 3$, $F = -49.78$, and $Pe = 1600$. Times are $t = 4$, 12, and 18. Also shown is the streamline pattern in the reference frame moving with the $c = 0.5$ contour at $t = 18$, as well as a sketch of its topology (*b*). A closed, toroidal recirculation region forms that leads to a 'pinch-off'-like phenomenon near the finger tip.

different topology (cf. figure 15*b*), with a saddle point located off the tube axis, but no stagnation point on the tube axis, so that fluid 1 can leak from the finger tip and form the 'needle shape' that is observed in the experiments of Part 1 as well. It should be pointed out that for steady, immiscible flow the above toplogical pattern does not represent a possible solution in the reference frame moving with the finger tip.

For $R = 3$, $F = -49.78$, and $Pe = 1600$, the topological complexity of the velocity field has further increased (figure 16), and we observe a toroidal, closed recirculation bubble inside the finger, as indicated in the sketch of the topological structure of the streamline pattern, cf. figure 16(*b*). As for the case depicted in figure 15, the streamline pattern in the reference frame moving with the $c = 0.5$ contour does not exhibit a stagnation point on the centreline, so that fluid continues to be ejected from the finger tip. Near the tip, the recirculation zone transports fluid 1 away from the centreline towards larger radii, thereby creating a steep concentration front on the side of the finger tip. A short distance further upstream, fluid is convected from larger to smaller radii, so that the concentration field appears headed towards a 'pinch-off' of the finger tip, i.e., the formation of a bubble. As discussed in Part 1, the dye

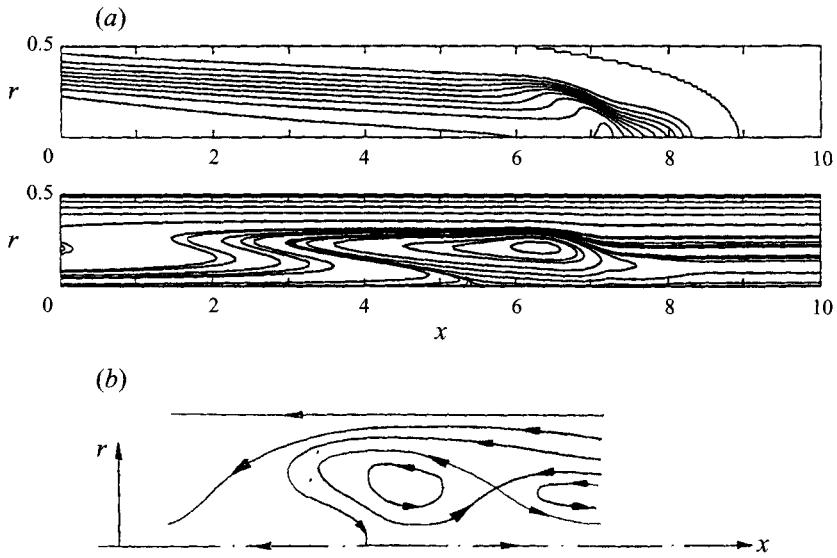

FIGURE 17. (*a*) Concentration field and streamfunction in the reference frame moving with $c = 0.5$ for $R = 5$, $F = -47.16$, and $Pe = 1600$, at $t = 15$. The topology of the streamline pattern is sketched in (*b*). The recirculation region persists. In addition, there now is a reverse-flow interval along the tube centreline. Since the propagation velocity of the $c = 0.5$ contour is less than one, an additional saddle has to exist on the axis, upstream of the computational domain.

patterns observed in corresponding experimental situations indicate the existence of a recirculation region near the finger tip as well.

For $R = 5$, $F = -47.16$, and $Pe = 1600$, the streamline pattern in the reference frame moving with the $c = 0.5$ contour still contains a closed recirculation region. It has now undergone an additional bifurcation, which has led to the existence of a reverse-flow interval along the centreline, cf. figure 17 at $t = 15$, and in particular figure 17(*b*). In spite of the reverse flow, fluid 1 leaks from the finger tip. As discussed above, an additional saddle has to exist upstream of the computational domain, where the centreline velocity approaches Poiseuille flow. However, this saddle can be located as far upstream as the root of the finger.

Figure 18 displays the finger tip velocity as a function of the gravity parameter F for different values of R. Over most of the F-interval, the (V_{tip}, F)-relationship follows a straight line reasonably closely, as shown by the least-squares fits in the figure. Furthermore, for $R \geqslant 3$ the slope of this linear relationship depends only very weakly on R. Figure 19 displays the (m, F)-data for the different values of R. In addition, the continuous relationships obtained by the least-squares fits to the data of figure 18 result in the curves provided in figure 19. For a comparison with the experimental data, see the discussion in Part 1.

4.2. $Pe \leqslant O(10^3)$

For this range of lower Pe values, the formation of a quasi-steady finger shape is not observed. Instead, as exemplified by the case of $Pe = 100, R = 5, F = 0$ (figure 20), diffusion soon causes the concentration front to decay, thereby resulting in a progressively more spread out finger tip. The computational results in figure 20 indicate that with time the concentration field becomes increasingly smoother. It is interesting to note that for $c \neq c(r)$, Poiseuille flow represents an exact solution to the

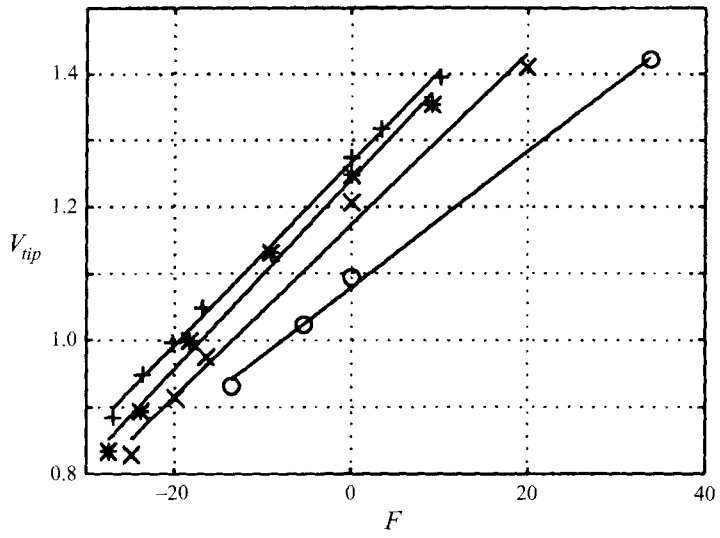

FIGURE 18. Tip velocity as a function of the gravity parameter F for different values of R. Over most of the F-interval, a linear relationship provides a reasonable fit to the data. o, R=2; ×, R=3; *, R=4; +, R=5.

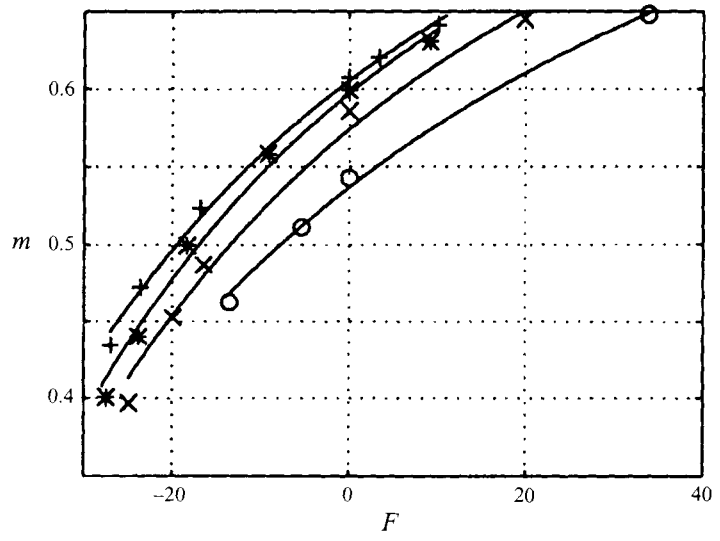

FIGURE 19. m, F-relationships for the different values of R, along with the least squares fits of figure 18. o, R=2; ×, R=3; *, R=4; +, R=5.

Navier–Stokes equations, independent of the x-dependence of the concentration. As a result, for small radial variations of c we expect Taylor's (1953) work on passive dispersion in Poiseuille flow to provide some guidance for the analysis of the flow development in the low-Pe regime. In particular, under the assumption that

$$\frac{\partial^2 c}{\partial x^2} \ll \frac{\partial^2 c}{\partial r^2} + \frac{1}{r}\frac{\partial c}{\partial r}, \tag{4.10}$$

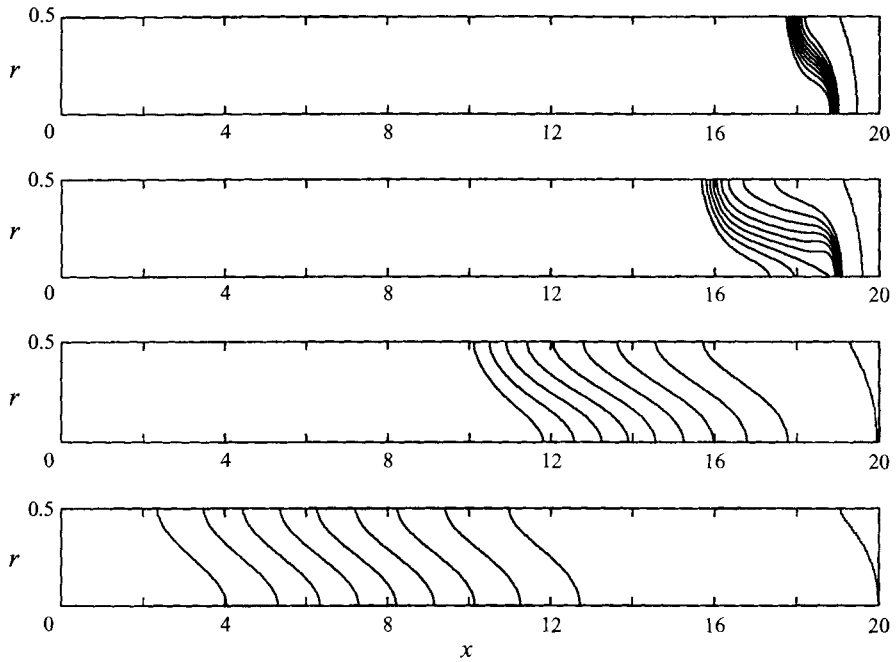

FIGURE 20. Evolution of the concentration field for $R = 5$, $F = 0$, and $Pe = 100$. Times are $t = 1$, 3, 10, and 25. At these low Pe values, the concentration front spreads diffusively, so that a quasi-steady state does not form.

i.e. that axial diffusion is much less significant than radial diffusion, Taylor shows that convective effects on the concentration field will be small compared to diffusive effects if

$$\frac{\delta}{d}\frac{58}{Pe} > C_2, \tag{4.11}$$

where δ is a measure of the thickness of the smeared out front, and $C_2 > 1$. Consequently, we would expect to see small concentration differences in the radial direction, and hence Poiseuille flow, once the dimensionless thickness of the smeared out front has reached a transitional range of values that increase linearly with Pe. If we take δ as the distance along the centreline between the 0.1 and 0.9 concentration contours, then figure 20 indicates that for $Pe = 100$ and $t = 10$ we have $58\delta/(Pe\,d) \approx 3.5$. Figure 21 shows the fluid velocity at the centreline location where the concentration averaged over the tube cross-section

$$c_m(x,t) = \frac{8}{d^2}\int_0^{d/2} rc(x,r,t)\mathrm{d}r \tag{4.12}$$

has the value of 0.5. The graph confirms that by this time the velocity has indeed decayed to near Poiseuille flow. The velocity field has become similarly close to Poiseuille flow for $Pe = 200$ and $t = 22$ (figure 22*a*), and for $Pe = 400$ and $t = 38$ (figure 22*b*), when $58\delta/(Pe\,d) \approx 3.5$ as well. These results confirm the above scaling considerations and indicate that $C_2 = 3.5$ is an appropriate value. We can hence conclude that Poiseuille flow will be reached approximately when

$$\frac{\delta}{d} \approx \frac{Pe}{16}. \tag{4.13}$$

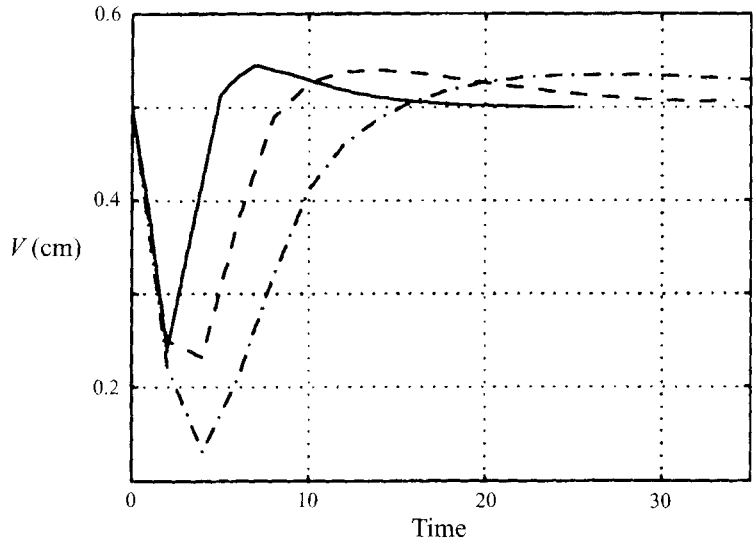

FIGURE 21. Propagation velocity of the x-location at which the concentration averaged over the cross-section $c_m(x,t) = 0.5$. $R = 5$, $F = 0$, and $Pe = 100$ (—), 200 (- - -), and 400 (- · - · -). In all cases the velocity asymptotically approaches the value of 0.5 predicted by Taylor (1953) for passive dispersion in Poiseuille flow.

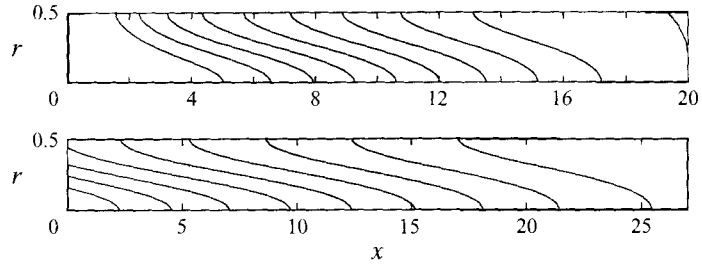

FIGURE 22. Concentration field for $R = 5$, $F = 0$, and: (*a*) $Pe = 200$ at $t = 20$, (*b*) $Pe = 400$ at $t = 38$.

Taylor furthermore provides an expression for δ as a function of time and what by now has become known as the Taylor dispersion coefficient k:

$$\delta = 3.62(kt)^{1/2}. \tag{4.14}$$

Here k is related to the tube diameter, the centreline velocity U of the Poiseuille flow, and the diffusion coefficient as

$$k = \frac{d^2U^2}{768D}. \tag{4.15}$$

With the above estimate (4.13) for δ/d by the time Poiseuille flow is reached, we can now estimate the *dimensionless time* it takes to approach Poiseuille flow. Notice that, strictly speaking, we estimate the time until Poiseuille flow is established on the basis of a relationship that assumes Poiseuille flow already exists. Nevertheless, as we will see below, this approach leads to reasonably good results. We obtain

$$t \approx 0.23Pe. \tag{4.16}$$

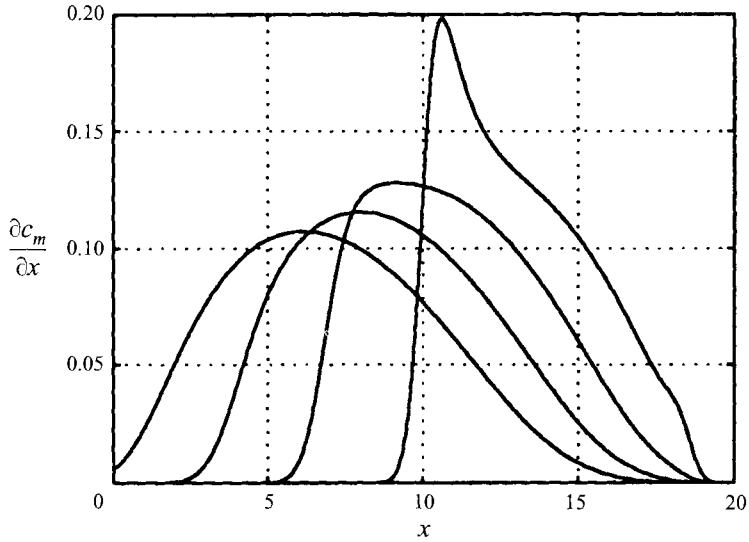

FIGURE 23. The derivative $\partial c_m/\partial x$ of the concentration averaged over the tube cross-section for $R = 5$ and $Pe = 100$. Times are $t = 10$, 15, 20, and 25. The profile asymptotically approaches a Gaussian shape, as predicted by Taylor (1953) for passive dispersion in Poiseuille flow.

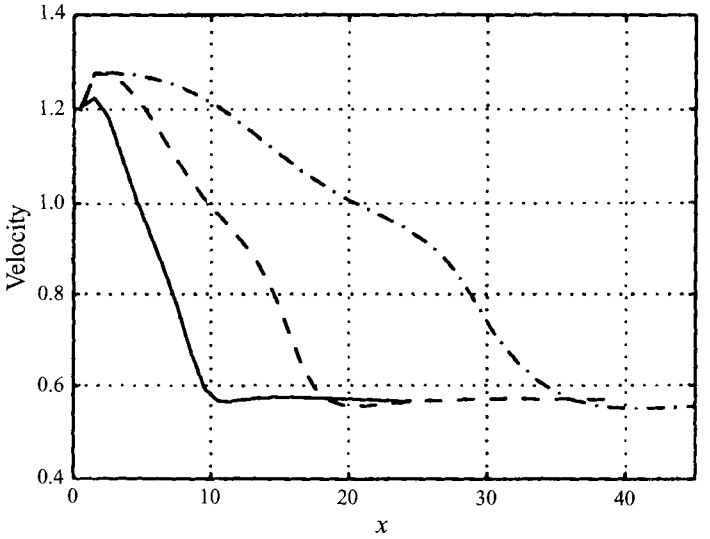

FIGURE 24. Propagation velocity of the x-location where $c = 0.9$. $R = 5$, $F = 0$, and $Pe = 100$ (—), 200 (- - -), and 400 (- · - · -), respectively. The time after which the asymptotic propagation velocity is approached increases linearly with Pe.

Consequently, after this time the cross-section-averaged concentration profile $c_m(x,t)$ should approach the shape of an error function. Equivalently, $\partial c_m/\partial x$ should take the form of a Gaussian. Figure 23 demonstrates this tendency, although at $t = 25$ the derivative of the concentration still exhibits a slight asymmetry. Figure 24 shows the propagation velocity of the $c = 0.9$ concentration contour for $Pe = 100$, 200, and 400, as a function of time. For all three cases, an asymptotic state is reached, after a time that increases linearly with Pe, in agreement with the above scaling arguments.

5. Variable diffusion coefficient

As discussed above, a comparison of the flow visualization experiments with the numerical simulations for the capillary tube shows good agreement for large values of Pe, while there are some discrepancies at lower values of this parameter. Specifically, in the experiments the film thickness attains its asymptotic state only for much higher values of Pe, typically $O(10^4)$, as compared to the simulations, where the value is closer to $O(10^3)$. For reasons discussed in Part 1, no experiments were conducted below Pe values of 10^3.

The experimental measurements of the diffusion coefficient between glycerine and the glycerine–water mixture in Part 1 display a pronounced asymmetry of the time-dependent concentration profile, in addition to a shift in the location of the maximum gradient. This indicates that the diffusion coefficient varies with the local concentration. Hence, in a more accurate simulation of the flow, Pe should be treated as a concentration-dependent parameter $Pe(c)$.

The experimentally measured one-dimensional concentration profiles in Part 1 provide some guidance towards quantifying the dependence of the diffusion coefficient D on the concentration c. For this purpose, we consider the one-dimensional diffusion equation

$$\frac{\partial c(x,t)}{\partial t} = \frac{\partial}{\partial x}\left(D(c)\frac{\partial c(x,t)}{\partial x}\right). \tag{5.1}$$

Rewriting it as

$$\frac{\partial c}{\partial t} - \left(\frac{\mathrm{d}D}{\mathrm{d}c}\frac{\partial c}{\partial x}\right)\frac{\partial c}{\partial x} = D(c)\frac{\partial^2 c}{\partial x^2} \tag{5.2}$$

demonstrates that the dependence of the diffusion coefficient on the concentration introduces a convection-like effect into the evolution equation for the concentration, with an effective local velocity

$$u_{eff}(x,t) = -\frac{\mathrm{d}D}{\mathrm{d}c}\frac{\partial c}{\partial x}. \tag{5.3}$$

In particular, the effective propagation velocity $u_{eff}|_{c_{xx}=0}$ of the concentration value at the inflection point, characterized by $c_{xx} = 0$, is given by

$$u|_{c_{xx}=0} = -\left.\frac{\mathrm{d}D}{\mathrm{d}c}\frac{\partial c}{\partial x}\right|_{c_{xx}=0}. \tag{5.4}$$

The experimental profiles at successive times can be used to estimate both this effective velocity and the instantaneous local concentration gradient, thereby providing us with an estimate of $\mathrm{d}D/\mathrm{d}c$ at the concentration value of the inflection point. This procedure can be repeated for mixtures of different glycerine concentrations in order to obtain estimates of $\mathrm{d}D/\mathrm{d}c$ at different concentrations. Figure 25 indicates that this quantity stays nearly constant over a wide range of concentrations, so that the assumption of a linear relationship between D and c

$$D(c) = D_0 + \frac{\mathrm{d}D}{\mathrm{d}c}c \tag{5.5}$$

represents a reasonably accurate first attempt at investigating the effect of a concentration-dependent diffusion coefficient on the overall finger dynamics. D_0 or, alternatively, the ratio a of the diffusion coefficients at $c = 0$ and $c = 1$ can be determined approximately by comparing the degree of asymmetry of the $\partial c/\partial x$-profiles at different times in one-dimensional test calculations with their experimental

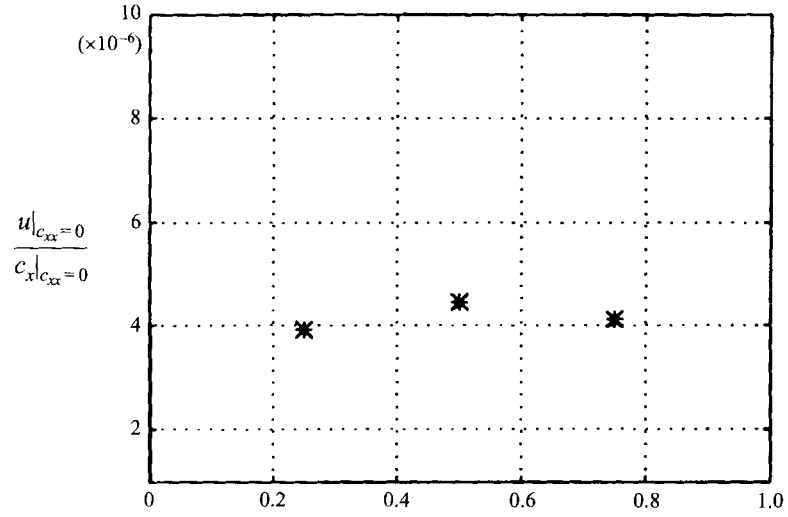

FIGURE 25. Estimated values of $u|_{c_{xx}=0}/c_x|_{c_{xx}=0}$ from experimental data for different times and concentrations. This nearly constant value suggests a linear relationship between D and c over a wide range of c.

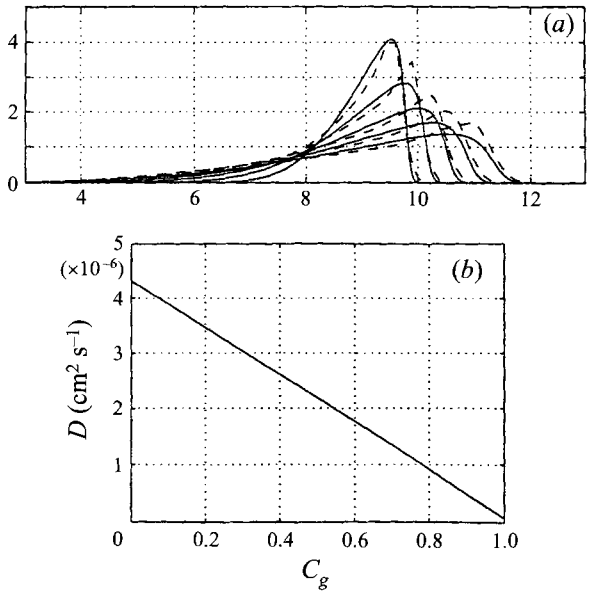

FIGURE 26. (*a*) Comparison of experimental (- - -) and numerical (—) one-dimensional $\partial c/\partial x$-profiles at different times for $a = 40$. The close agreement validates the assumption of a linear (D, c)-relationship. (*b*) Diffusion coefficient in a water–glycerine mixture, as a function of the local concentration.

counterparts. Figure 26(*a*) shows such a comparison of experimental and numerical $\partial c/\partial x$-profiles at different times for $R = 5.52$ and $a = 40$, indicating that the assumption of a linear (D, c)-relationship works reasonably well. The resulting (D, c)-relationship, shown in figure 26(*b*), agrees reasonably well with the experimental estimates in Part 1, where, in a slightly different way, was an estimate of $a = 26.5$ (cf. their figure 5).

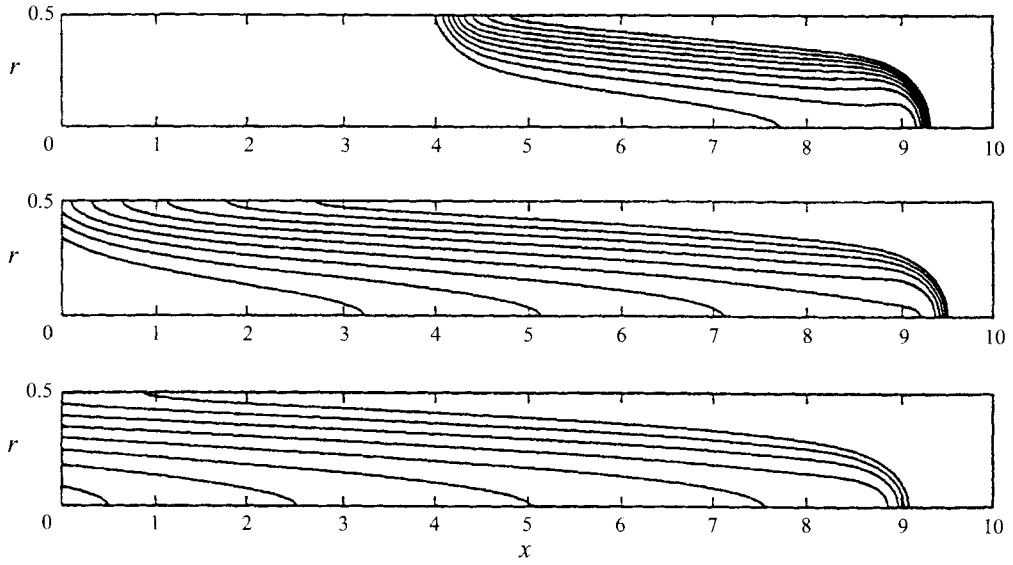

FIGURE 27. Evolution of the concentration field for R=5.52 with time for times 5, 10 and 15. The diffusion coefficient is concentration dependent, so that the value of Pe varies between 195 and approximately 4000 across the front.

The variation of the diffusion coefficient by a factor of $O(40)$ across the concentration front allows for the development of fingers with a smooth variation of the concentration in the interior, and well-defined sharp outer edges, as seen in figure 27 for $R = 5.52$, corresponding to the displacement of glycerine by a 50%-mixture of glycerine and water. The ratio a of the diffusion coefficients in the mixture and in pure glycerine is about 20, so that Pe varies between 195 and approximately 4000 across the front. While the finger maintains a steep leading edge for a fairly long time, its tip velocity does not exhibit the plateau-like nature characteristic of a quasi-steady state.

6. Additional stresses in miscible flows

As discussed earlier, the assumption of vanishing divergence represents an approximation for miscible fluids of different densities. In the following, we will attempt to predict in which parameter regimes the additional stresses related to this effect will be most pronounced. For the purpose of estimating the relative importance of the stresses related to the divergence of the velocity field, we assume that these stresses are related to the magnitude of the divergence by a constant proportionality factor δ. Following Joseph & Hu (1991), we can estimate the magnitude of the divergence of the velocity vector as

$$\nabla \cdot \boldsymbol{u} = \frac{\rho_1 - \rho_2}{\rho_1} \nabla \cdot [D(c) \nabla c]. \tag{6.1}$$

If we assume that, to a first approximation, D is constant and $\rho_1 - \rho_2 \sim c_1 - c_2 = \Delta c$, we obtain

$$\nabla \cdot \boldsymbol{u} \sim (c_1 - c_2) D \nabla^2 c. \tag{6.2}$$

This effect is expected to be largest where the concentration front is steepest, i.e. near the finger tip. In order to estimate $\partial^2 c / \partial x^2$ at the finger tip, we can employ the

same one-dimensional convection–diffusion model used above to estimate the front thickness δ_0. We find

$$c_{xx} \sim \frac{\Delta c}{\delta_0^2} \sim \frac{V_{tip}\Delta c}{Dd} \tag{6.3}$$

where d denotes the tube diameter, which results in

$$\nabla \cdot \boldsymbol{u} \sim (\Delta c)^2 \frac{V_{tip}}{d}. \tag{6.4}$$

Both Δc and V_{tip}/d increase as $At \to 1$, so that the related stress should reach its largest value in this limit.

For the second source of additional stresses in miscible liquids mentioned above, i.e. the different chemical potentials of the two liquids, scaling considerations can prove helpful as well. For the pressure jump across a spherical miscible interface due to the chemical potential effect we follow Davis (1988) as well as Joseph & Hu (1991) and write

$$\Delta p \sim \sigma \int_{r_1}^{r_2} \frac{c_r^2}{r} \mathrm{d}r \tag{6.5}$$

where σ is a material constant, and r_1 and r_2 are on opposite sides of the concentration layer. For scaling purposes, the axisymmetric tip of the finger in the capillary tube can be approximated as being locally spherical. Furthermore, since the thickness of the concentration layer at the finger tip is much smaller than the finger tip radius, the factor $1/r$ can be pulled out of the integral. By again employing our earlier estimate of the concentration layer thickness from a balance of strain and diffusion, we obtain

$$c_r \approx \frac{\Delta c}{\delta_0}, \qquad \delta_0 \sim \left(\frac{D}{\alpha}\right)^{1/2}, \qquad \alpha \sim \frac{V_{tip}}{d}. \tag{6.6}$$

For the pressure difference across the finger tip, this results in

$$\Delta p \sim \sigma \frac{(\Delta c)^2}{d^2} \left(\frac{V_{tip} d}{D}\right)^{1/2} \tag{6.7}$$

$$\sim \sigma \frac{(\Delta c)^2}{d^2} (Pe)^{1/2}. \tag{6.8}$$

Consequently, the additional stresses in the form of a pressure difference related to the chemical potential should be most pronounced as $At \to 1$ and Pe increases.

Both of the above extra stress terms reach their largest values as $At \to 1$ and Pe increases, which is the regime where we observe very good agreement between the numerical simulations and the experiments in Part 1. However, this cannot be interpreted as conclusive evidence that the extra stress terms are unimportant. In order to evaluate their relevance in the present flow, it is helpful to evaluate their relative strength as compared to the viscous stresses, which are also expected to reach maximum values when steep fronts exist in the flow. A representative term of the viscous stress tensor is

$$\tau \sim \frac{\partial}{\partial x}\left(\mu \frac{\partial u}{\partial x}\right). \tag{6.9}$$

At the finger tip we can again approximate the velocity field as that of a stagnation point, so that u depends linearly on x, which leads to

$$\tau \sim \frac{\mathrm{d}\mu}{\mathrm{d}c} \frac{\partial c}{\partial x} \frac{\partial u}{\partial x}. \tag{6.10}$$

With the same estimate for the strain field as above, and with $\mu_2 \gg \mu_1$, this results in

$$\tau \sim \mu_2 (Pe)^{1/2} \frac{V_{tip}}{d^2}. \tag{6.11}$$

For the ratio of stresses induced by the different chemical potentials and viscous stresses, we thus obtain

$$\frac{\Delta p}{\tau} \sim \frac{\sigma (\Delta c)^2}{\mu_2 V_{tip}}. \tag{6.12}$$

This ratio increases as the viscosity of the displaced fluid and the tip velocity decrease, i.e. with decreasing Pe and At. Similarly, the ratio of stresses due to divergence in the velocity field and viscous stresses scales as

$$\frac{\delta \nabla \cdot \boldsymbol{u}}{\tau} \sim \frac{\delta (\Delta c)^2 d}{\mu_2 (Pe)^{1/2}}. \tag{6.13}$$

Again, the omitted stresses due to the divergence of the velocity field increase in relative importance with decreasing Pe and At. The above arguments indicate that the extra stresses analysed by Joseph and coworkers, when compared to the viscous stresses, can become relatively more important in those flow regimes where steep fronts *do not* exist. In the regime of large Pe and At, we observe very good agreement between our simulations, which omit these stresses, and the experiments in Part 1. However, for smaller values of these parameters some differences between the two exist, and we cannot exclude the possibility that they are at least partially due to the influence of these extra stresses.

7. Conclusions

The present computational research effort, in conjunction with the accompanying experiments in Part 1, has been directed at elucidating the dynamics of miscible displacement processes in capillary tubes and, to a lesser extent, in plane two-dimensional channels. Based on the Stokes equations, we investigated the flow that is generated if a fluid of given viscosity and density displaces a second fluid of different such properties. The main dimensionless quantities are the Péclet number, the Atwood number, and a gravity parameter. Further dimensionless parameters arise from the dependence on the concentration of various physical properties, such as viscosity and the diffusion coefficient. Strict dynamical similarity can be obtained only if all of these parameters are matched in different experiments. However, the behaviour of most of the global quantities of practical interest, such as the fraction of displaced fluid left behind, is usually dominated by Pe, At, and F.

One of the main findings concerns the identification of two distinct Pe regimes, which are separated by a transitional region. For large values of Pe, typically above $O(10^3)$, we observe the formation of a quasi-steady flow near the finger tip, which is characterized by a sharp concentration front. Scaling laws for the front thickness and the maximum concentration gradient show good agreement with the numerical results. This quasi-steady state persists until the time it takes the finger to reach a certain length that is proportional to Pe. Around this time, the concentration layers on the side of the finger begin to diffuse into each other, thereby cutting off the supply of uncontaminated displacing fluid. Eventually, the initially steep concentration fronts will decay and Poiseuille flow with Taylor dispersion will develop asymptotically.

In the small-Pe regime, typically below $O(10^3)$, the quasi-steady state never forms, and the flow asymptotically approaches Taylor dispersion from the start. For this case, a scaling law for the time it takes to reach Poiseuille flow and Taylor dispersion exhibits good agreement with the numerical data.

For the large-Pe regime, we find close agreement between the simulations and the accompanying experiments in Part 1. This is exemplified by the data for the film thickness as a function of At, in the limit of large Pe. Depending on the importance of gravitational forces, the finger tip velocity can be larger or smaller than the centreline velocity of the unperturbed Poiseuille flow. Accordingly, we find a variety of accompanying streamline patterns near the finger tip, among them those outlined by Taylor (1961) for immiscible flows. In particular, for some parameters closed toroidal recirculation zones inside the finger tip are observed, which can explain the experimentally observed deformations of the interface between the dye and the clear fluid.

In order to clarify the remaining differences between experimental and numerical observations, we focused on several potentially important issues: First, we considered the concentration dependence of the diffusion coefficient. Experimental data in Part 1 indicate that D can be smaller by a factor of $O(30)$ in nearly pure glycerine than in nearly pure water. By incorporating this $D(c)$ dependence into the numerical simulations, we observed the evolution of fingers that exhibited steep external concentration fronts along with smooth concentration fields on the inside of the finger, at moderate values of Pe. Another point concerns the viscosity–concentration relationship. In the numerical simulations, we assumed an exponential behaviour, in line with earlier investigations by other authors. For the particular liquids employed in the experiments, on the other hand, it is pointed out in Part 1 that for glycerine concentrations above 0.2, the viscosity of the mixture depends on the concentration in a nearly double-exponential fashion. For large values of Pe, the exact form of the relationship is not expected to be of much importance, as its effects are limited to very thin concentration layers. At small Pe, on the other hand, concentration gradients occur in large portions of the flow field, and the details of the (μ, c)-relationship could have a more significant effect.

Additional sources of discrepancies between experiments and simulations concern the potential effect of Korteweg stresses, as well as the approximative nature of the assumption of a divergence-free velocity field. Straightforward scaling arguments indicate that these stresses should be strongest when steep concentration fronts exist, i.e. at large values of Pe and At. However, their *relative* importance compared to viscous stresses may be larger at lower values of these parameters, and we cannot exclude the possibility that the discrepancies we observe between experiments and simulations in this regime are partially due to these effects.

This work was made possible through support by the Department of Energy, Office of Basic Energy Sciences, under grant DE-FG03-93ER-14346. Also, the support through a NATO Collaborative Research Grant is gratefully acknowledged. We deeply appreciate the contributions made to this work by our collaborators Prof. Tony Maxworthy and Dr. Philippe Petitjeans. Furthermore, we had several helpful discussions with Prof. Yanis Yortsos. We would also like to thank Prof. Salin for making a preprint of his work available to us, and one of the reviewers for helpful comments regarding the importance of the Korteweg stresses. Supercomputing resources have been provided by the San Diego Supercomputer Centre.

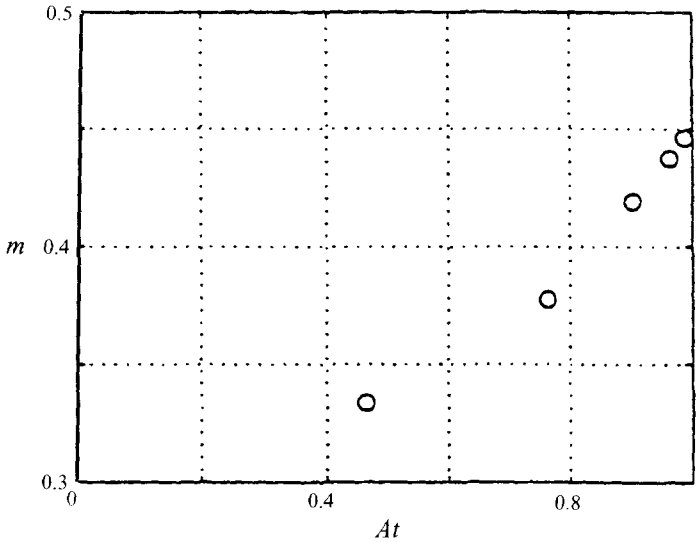

FIGURE 28. Fraction of the displaced fluid left behind on the channel wall, as a function of the viscosity ratio for $Pe = 1600$ and $F = 0$. Apart from a shift by a constant value of 1/6, the curves for the round tube (figure 7) and the plane channel display the same shape.

Appendix. Two-dimensional flow in plane channel

For the two-dimensional flow in a plane channel, a corresponding set of governing equations and boundary conditions holds. Again, the equations are most conveniently solved by casting them into a streamfunction–vorticity formulation. The same numerical solution procedures as for the capillary tube case can then be applied, along with the corresponding computational inflow and outflow boundary conditions. While our observations for the plane channel flow overall are similar to those described above for the capillary tube, it is worthwhile to discuss a few of the results in more detail.

As for the capillary tube, we observe quasi-steady fingers for large values of Pe. A corresponding scaling assumption for the strain

$$\alpha \approx \frac{4(V_{tip} - U)}{h} \tag{A 1}$$

where h denotes the channel width, leads to an estimate for the maximum finger length

$$\frac{L_f}{h} \approx 0.296Pe. \tag{A 2}$$

By again carrying out an extrapolation procedure in order to obtain asymptotic values for the film thickness as a function of the viscosity ratio, we arrive at the (m, At)-relationship depicted in figure 28. An interesting similarity exists between the (m, At) curves for the round tube and the plane channel. After adjusting for the difference in film thicknesses at $At = 0$, the curves collapse to within the accuracy of the numerical data.

If gravity is included in the simulations, similar effects are observed as in the round tube case. In particular, it is found that the topological transition leading to the emergence of a thin protrusion from the finger tip exists for the plane channel flow as well. Figure 29 shows an example of the concentration and streamline patterns for $R = 3, F = -51.8$, and $Pe = 1600$ which demonstrates the existence of several closed

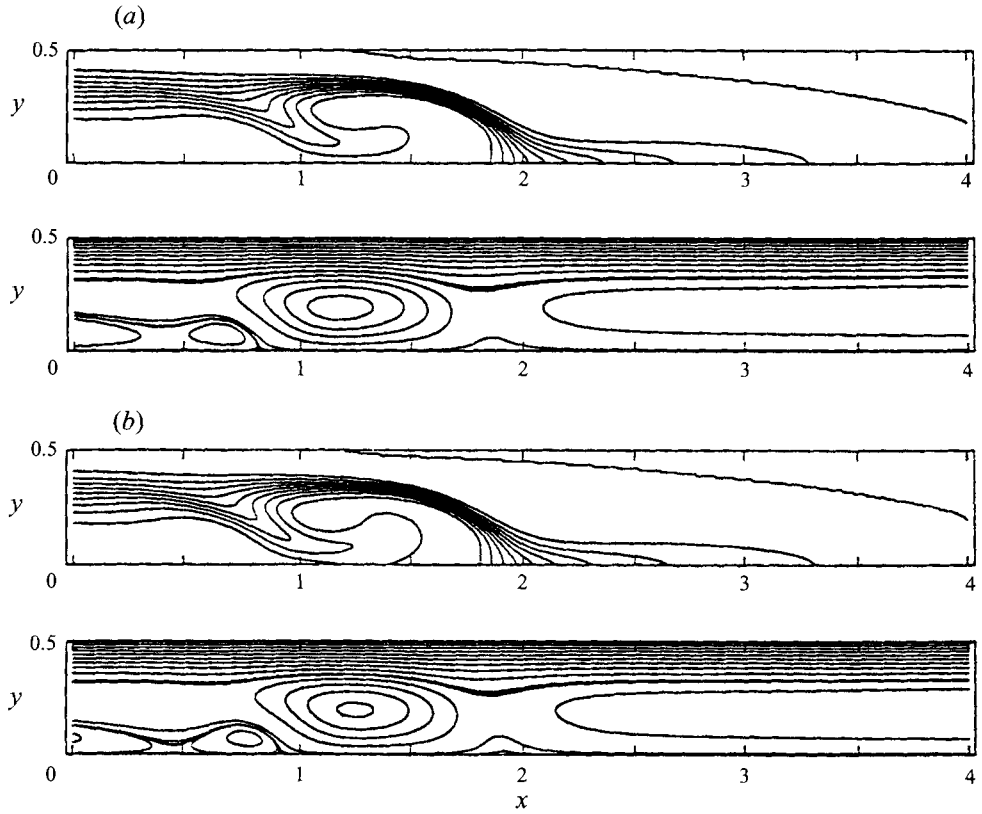

FIGURE 29. Unsteady evolution of the concentration field for $R = 3$, $F = -51.8$, and $Pe = 1600$ for flow in a plane channel. Times are (*a*) $t = 14$ and (*b*) 15. Also shown are the streamline patterns in the reference frame moving with the $c = 0.5$ contour. Similarly to the capillary tube, closed recirculation regions form, leading to a 'pinch-off'-like phenomenon near the finger tip.

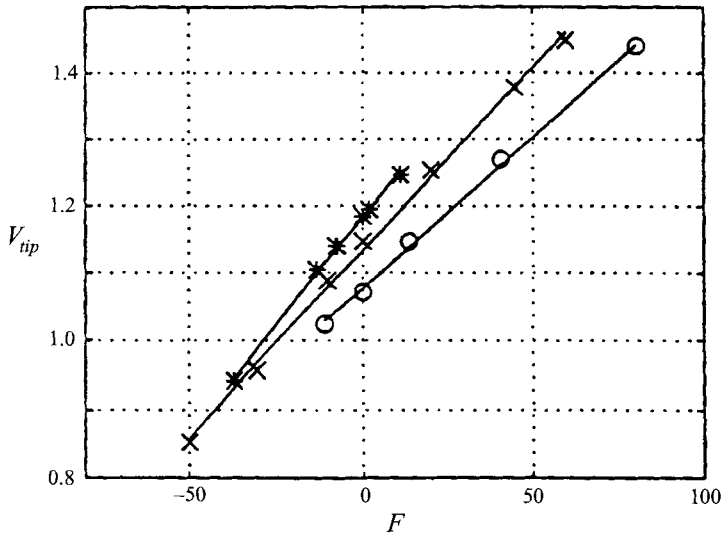

FIGURE 30. Tip velocity in the plane channel flow as a function of the gravity parameter F for different values of R. Over most of the F-interval, a linear relationship provides a reasonable fit to the data. o, R=2; ×, R=3; *, R=4.

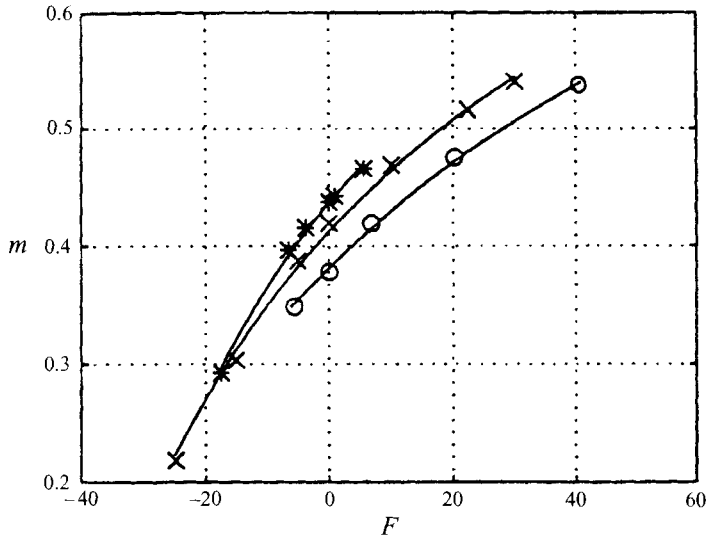

FIGURE 31. m, F-relationships for the different values of R, along with the least-squares fits of figure 30. o, $R=2$; ×, $R=3$; *, $R=4$.

recirculation regions within the finger. Over the range of gravity parameter values explored, the finger tip velocity again varies in a nearly linear fashion (figure 30), and we can obtain reasonably accurate least-squares fits of straight lines. These in turn lead to the (m, F) curves shown in figure 31.

In order to derive the relevant scaling laws for the diffusion-dominated regime of lower Pe values, one can repeat Taylor's (1953) analysis of dispersion in a round tube for plane channels. The resulting effective Taylor dispersion coefficient given by Horne & Rodriguez (1983) is

$$k = \frac{2U^2h^2}{945D}. \tag{A 3}$$

It leads to an estimated dimensionless time to approach Poiseuille flow of

$$t \approx 0.4Pe \tag{A 4}$$

which is quite similar to the result for flow in a capillary tube. Again, these scaling results are confirmed by the simulations.

REFERENCES

BRANDT, A. 1977 Multi-level adaptive solutions to boundary-value problems. *Math. Comput.* **31**, 333.

BRETHERTON, F. P. 1961 The motion of long bubbles in tubes. *J. Fluid Mech.* **10**, 166.

COX, B. G. 1962 On driving a viscous fluid out of a tube. *J. Fluid Mech.* **14**, 81.

DAVIS, H. T. 1988 A theory of tension at a miscible displacement front. In *Numerical Simulation in Oil Recovery*. IMA Volumes in Mathematics and Its Applications 11 (ed. M. Wheeler). Springer.

FLETCHER, C. A. J. 1988 *Computational Techniques for Fluid Dynamics*, Vol. 1. Springer.

HORNE, R. H. & RODRIGUEZ, F. 1983 Dispersion in tracer flow in fractured geothermal systems. *Geophys. Res. Lett.* **10**, 289.

JOSEPH, D. D. 1990 Fluid dynamics of two miscible liquids with diffusion and gradient stresses. *Eur. J. Mech.* B/*Fluids* **9**, 565.

JOSEPH, D. D. & HU, H. 1991 Interfacial tension between miscible liquids. Army High Performance Computing Research Centre, University of Minnesota, preprint 91–58.

JOSEPH, D. D. & RENARDY, Y. Y. 1993 *Fundamentals of Two-Fluid Dynamics. Part II. Lubricated Transport, Drops, and Miscible Liquids*. Springer.

KORTEWEG, D. 1901 Sur la forme que prennent les équations du mouvement des fluides si l'on tient compte des forces capillaires causées par des variations de densité. *Arch. Neerl. Sci. Ex. Nat.*, (II), **6**, 1.

PETITJEANS, P. & MAXWORTHY, T. 1996 Miscible displacements in a capillary tube. Part 1. Experiments. *J. Fluid Mech.* **326**, 37 (referred to herein as Part 1).

RAKOTOMALALA, N., SALIN, D. & WATZKY, P. 1996 Miscible displacement between two parallel plates: BGK Lattice gas simulations. Submitted to *J. Fluid Mech.*

REINELT, D. A. & SAFFMAN, P. G. 1985 The penetration of a finger into a viscous fluid in a channel and tube. *SIAM J. Sci. Statist. Comput.* **6**, 542.

ROGERSON, A. M. & MEIBURG, E. 1993*a* Shear stabilization of miscible displacement processes in porous media. *Phys. Fluids* A **5**, 1344.

ROGERSON, A. M. & MEIBURG, E. 1993*b* Numerical simulation of miscible displacementprocesses in porous media flows under gravity. *Phys. Fluids* A **5**, 2644.

TAN, C. T. & HOMSY, G. M.1986 Stability of miscible displacements in porous media: Rectilinear flow. *Phys. Fluids* **29**, 3549.

TAYLOR, G. I. 1953 Dispersion of soluble matter in solvent flowing slowly througha tube. *Proc. R. Soc. Lond.* A **219**, 186.

TAYLOR, G. I. 1961 Deposition of a viscous fluid on the wall of a tube. *J. Fluid Mech.* **10**, 161.

YANG, Z. & YORTSOS, Y. C. 1996 Asymptotic solutions of miscible displacements ingeometries of large aspect ratio. Submitted to *Phys. Fluids.*